

The Pennsylvania State University
The Graduate School
College of Engineering

LOW-COST THERMOACOUSTIC COGENERATOR FOR USE IN BIO-MASS BURNING COOK STOVES

A Thesis in
Mechanical Engineering
By
Paul J. Montgomery, Jr.

© 2010 Paul J. Montgomery, Jr.

Submitted in Partial Fulfillment
of the Requirements
for the Degree of
Master of Science

December 2010

The thesis of Paul J. Montgomery, Jr. was reviewed and approved* by the following:

Karen A. Thole
Professor of Mechanical Engineering
Head of the Department of Mechanical Engineering

Steven L. Garrett
Professor of Acoustics
Thesis Co-Advisor

Horacio Perez-Blanco
Professor of Mechanical Engineering
Thesis Co-Advisor

Robert J. Santoro
Professor of Mechanical Engineering

*Signatures are on file in the Graduate School

LOW-COST THERMOACOUSTIC COGENERATOR FOR USE IN BIO-MASS BURNING COOK STOVES

ABSTRACT

Indoor smoke produced while cooking using bio-mass fuel causes 1.6 million premature deaths every year; one million children die of pneumonia and 600,000 women die prematurely of chronic obstructive pulmonary diseases like bronchitis and emphysema. This corresponds to 38 million disability-adjusted lost years in addition to needless pain and suffering from increased eye and respiratory illnesses. Worldwide, black carbon particulate matter (soot) is second only to carbon dioxide as an anthropogenic contributor to global warming in the atmosphere (direct radiative forcing) and also accelerates glacial and snowpack loss due to the melting caused by reduced albedo. In South-East Asia, soot can make a more significant contribution to global warming than carbon dioxide. With 2.53 billion humans using biomass as their primary cooking fuel, biomass-fired cook stoves account for 75% of that soot. 1.6 billion of these cook stove users live in villages that have no electricity.

An improved cook stove addresses both of these problems, but because the atmospheric lifetimes of black carbon particles is only a week or two, instead of 100 years for carbon dioxide (CO_2), 114 years for nitrous oxide (NO_2), and 12 years for methane (CH_4), atmospheric soot reduction is the only remediation activity that can produce immediate benefits.

Recent research has shown that fan-enhanced convection in the biomass combustion chamber makes the most significant reduction in the products of incomplete combustion that degrades indoor air quality and also is most successful in reduction of soot production. This prototype will utilize a thermoacoustic engine to extract a small amount of heat, generate a standing sound wave thermoacoustically, and use that sound wave to drive a loudspeaker-like linear alternator to generate electricity. Since the fan typically consumes only one watt and a simple thermoacoustic generator could produce 5-10 watts of electrical power, the excess electrical power can be used to provide lighting using a high-efficiency LED lamp, charge a mobile phone or other small electronic device, or run a small appliance.

Thermoacoustics seems like a potential candidate for low-cost electrical power generation because it is so simple and requires no moving parts other than the loudspeaker which must reciprocate to generate electrical power. The design and fabrication of a low-cost thermoacoustic power generator presented many challenges.

The prototype described herein used air at atmospheric pressure as the thermodynamic working gas. This choice allowed the hot-duct of the resonator to be constructed from folded sheet steel producing a rectangular cross-section instead of the circular cross-section typical of vessels designed to contain gases at higher pressures. The rectangular cross-section meant that the ceramic “stack” could also have a large-aspect rectangular cross-section (*i.e.*, very wide, but not too tall) so that the heat leaving the engine would not have to travel very far to reach the ambient temperature reservoir. This made the ambient heat exchanger simple but efficient. Cooling fins sold to cool computer chips were used to remove heat from the stack. The exhaust heat collected by the fins was measured by determining the rate at which ice melted in the “pool” above the ambient temperature portion of the resonator. By

coating the hot-end of the ceramic stack with carbon black from a candle, about 20 watts of heat was deposited on the stack directly by electromagnetic radiation making a hot heat exchanger unnecessary.

Experiments demonstrated that under similar conditions, the amplitude of the thermoacoustically-generated pressure increased for shorter stacks with larger ratios of pore size to thermal penetration depth in a resonator with smaller volume corresponding to larger gas stiffness.

A loudspeaker was sealed to the ambient end of the resonator and utilized its moving mass, in conjunction with the gas stiffness in the duct, to create a Helmholtz-like resonator that was more compact than a standing-wave resonator operating at the same frequency. Although the overall efficiency of thermal to electrical power conversion was fairly poor in this prototype, and only 18-26 mW of useful electrical power was extracted. This low output level was due, in part, to the fairly large mechanical resistance of the commercial loudspeakers.

This effort has proven that several of our innovations were workable and provides guidance for design of a second-generation device.

TABLE OF CONTENTS

List of Tables	vii
List of Figures	viii
List of Abbreviations.....	ix
Acknowledgements.....	x
Chapter 1: INTRODUCTION	1
1.1 Motivation	2
1.2 Objectives	6
1.3 Design Constraints and Challenges.....	6
1.4 Basic Thermoacoustic Theory	7
Chapter 2: ENGINE DESIGN AND BUILDING PROCESS	10
2.1 Mock Stove	10
2.2 Initial Computational Modeling.....	11
2.3 Hot-Side Duct.....	12
2.4 Ambient Temperature Duct.....	14
2.5 Heat Exchanger	16
2.6 Instrument Ports.....	16
2.7 Linear Alternators	17
2.8 Entire Assembly	19
Chapter 3: EXPERIMENTAL METHODS.....	20
3.1 Testing Instruments	20
3.2 Lab Bench Setup.....	23
Chapter 4: HEAT TRANSFER DATA	25
4.1 Assumptions.....	26
4.2 Radiant Heat Transfer	26
4.3 Conductive Heat Transfer	27
4.4 Latent Heat Transfer	27
4.5 Results.....	28
Chapter 5: HELMHOLTZ RESONATOR	31
5.1 Pre-Onset Free-Decay.....	32
5.2 Onset Data	35
Chapter 6: THERMOACOUSTIC ENGINE	41
6.1 Pre-Onset Free-Decay.....	41
6.2 Onset Data	43
Chapter 7: CONCLUSION	48
Bibliography	49
Appendix A: Initial DELTAEC code.....	52
Appendix B: Piezo-resistive microphone calibration	55
Appendix C: Survey of commercially available drivers	56

Appendix D.1: Dayton DA115-8 manufacturer's specifications	57
Appendix D.2: Dayton ND105-4 manufacturer's specifications	58
Appendix E: Helmholtz mode DELTAEC code	59
Appendix F: Power extraction mode DELTAEC code	61

LIST OF TABLES

1. Parameter measurements of electrodynamic speakers.....	18
2. Channel list for the multiplexed HP 34970A data acquisition and switch unit.....	21
3. Heat transfer parameter results	30
4. Helmholtz mode quality factor measurements at ambient temperatures	35
5. Lautrec numbers of different Celcor stack cell densities.....	38
6. Overview of Helmholtz mode resonator tests.....	40
7. Mechanical and electrical power dissipation.....	44
8. Overall power extraction tests.....	46

LIST OF FIGURES

1. Pollution effects of using biomass fuel for cooking	2
2. Pollutant results of different cook stove systems.....	4
3. Global warming/cooling potential of different stove systems	5
4. Celcor stack material (stock).....	7
5. Thermoacoustic cycle.....	8
6. Thermoacoustic demonstration device	9
7. Mock-stove assembly.....	11
8. SolidWorks™ model of engine	12
9. Hot duct TIG welds.....	13
10. Hot duct assembly.....	14
11. Flange, sides, bottom wall of ambient temperature duct	15
12. Aluminum heat exchanger	16
13. Instrument portal caps.....	17
14. DA115-8 and ND105-4 loudspeakers.....	18
15. DA115-8 with plunger volume exclusion device.....	19
16. Experimental thermoacoustic engine assembly	19
17. LabVIEW user input.....	22
18. LabVIEW user monitoring system	22
19. Lab bench experimental setup for engine	23
20. Lab bench overview during experimentation	24
21. Typical resonator temperature measurements during testing	25
22. Latent heat measurements.....	28
23. Experimental versus theoretical hot-side stack temperatures.....	29
24. Radiant heat transfer rate into stack	30
25. Pre-Onset 1/Q measurements	33
26. Experimental and theoretical decay waveform voltages	34
27. 1/Q PreOnset measurements	34
28. Onset frequencies and pressure magnitudes for various resonator neck lengths.....	36
29. Pressure magnitudes varying stack length.....	37
30. Pressure magnitudes varying stack density	38
31. Switch-box circuit schematic.....	39
32. Example of free decay of linear alternator in resonator.....	39
33. Circuit schematic for trigger mechanism	41
34. Example of free-decay raw data	42
35. Power extraction curves for set of experimental data	43
36. Power extraction varying stack cell density.....	44
37. Power extraction curves varying volume exclusion using DA115-8 driver.....	45
38. Power extraction curves varying volume exclusion using ND105-4 driver.....	46
39. DELTAEC and experimental power extraction curves	47

LIST OF ABBREVIATIONS

1. Combined-cycle heat and power (CHP)	1
2. Thermoelectric (TE).....	1
3. Intergovernmental Panel on Climate Change (IPCC)	3
4. Metal Inert Gas (MIG)	11
5. Tungsten Inert Gas (TIG)	12
6. Polyvinyl carbonate (PVC).....	13
7. Data acquisition/switch unit (DAQ)	19
8. Alternating current (AC).....	19
9. Direct current (DC).....	19
10. Thermocouple (TC).....	23
11. Digital Signal Oscilloscope (DSO).....	30

ACKNOWLEDGEMENTS

Thanks to the faculty and staff in the Mechanical Engineering Department and the Graduate Program in Acoustics for providing me with an academically stimulating environment. I would especially like to thank my advisor Dr. Steven Garrett for taking me onto this project and introducing me to a technology that may potentially make a significant difference to billions of people around the world, and my co-adviser Dr. Horacio Perez-Blanco for his guidance.

Finally, I would like to thank the Paul S. Veneklasen Research Foundation for their very generous gift that provided financial support for this research.

CHAPTER 1 INTRODUCTION

Today, there is unanimous agreement that innovative technology must be exploited to extract the greatest possible service from combustion of fuels in biomass burning cook stoves to increase overall energy efficiency and reduce the amounts of biomass required as input as well as reducing the pollutant by-products that represent a major source of indoor and atmospheric air pollution. This is leading to various strategies that improve the combustion process and provide the opportunity to “recycle” the waste heat.¹

At the smaller-scale end, micro-level combined-cycle heat and power (CHP) units for domestic applications are starting to gain acceptance. Those typically produce several kilowatts (~10,000 BTU/hr) of space-heating along with about one kilowatt of electrical power.² This thesis project will attempt to create electrical power at a scale that is over one-hundred times smaller. Although a thermoacoustic co-generation cook stoves would each produce only the order of a few watts of electrical power, there are probably two billion biomass-fueled cook stoves in use worldwide that might benefit from nano-CHP technology.

At such a small scale, the challenges are greatest because the smaller power generation must be provided at proportionately smaller unit cost. Very little research has been done on combustion or electrical energy production at that scale. Of that effort, almost all has thus far been directed to use of low-efficiency thermoelectric (TE) modules. Both the capture of the waste heat and its utilization at this scale presents challenges in thermal design and heat transfer, as well as small-scale heat engine cycles.

Equally challenging is the conversion of the captured waste heat from mechanical energy into electricity. The simplest approach involves a thermoelectric module and some mechanism to cool the cold-side positive/negative junctions, typically a fan-cooled finned aluminum heat sink. This approach is already being developed in the laboratory³ and field tested⁴, but questions about the robustness of the bismuth-telluride TE material's brittleness and hygroscopic tendency during rough handling in high humidity regions have not been established.

Although a solid-state conversion approach is attractive (*i.e.*, no moving parts), thermoelectric conversion efficiency is quite low; on the order of 3% or less without inclusion of the energy consumption of a fan that is used to cool the cold-junctions' heat sink. Almost any mechanical approach (*e.g.*, free-piston Stirling, Rankine micro-turbine⁵, or thermoacoustic⁶) has at least three times the efficiency of a thermoelectric converter. Of course, the additional mechanical complexity introduced by a simple linear alternator (*i.e.*, a loudspeaker operating as a linear alternator) introduces other limitations and cost constraint.

Philanthropic organizations⁷ and individuals have developed cook-stove improvements for economically disadvantaged communities in developing countries. There exist associations, both in the US⁸ and in Asia⁹, dedicated to sharing the solutions that have been developed and taken to different levels of demonstration. Just recently, the United Nations Foundation has launched its *Alliance for Clean Cook Stoves*¹⁰ with its first milestone being the deployment of 100 million improved stoves by 2020. Unfortunately, there is not nearly as much activity in development of small prime movers (*i.e.*, heat engines that generate mechanical power), especially those that use external combustion and tolerate variability in both fuel type and quality, while having the capability to generate less than 10 watts of electrical power.

1.1 Motivation

With nearly one-third of the Earth's population using biomass or coal-fueled cook stoves, the impact of their use on health and climate change is significant. Since biomass is a carbon-neutral renewable energy resource, it has the potential to reduce global warming if it is consumed efficiently and soot production is suppressed.

A major problem in developing countries is the use of low-quality biomass fuels in poorly ventilated cook stoves to provide space heating and cooking. This combination leads to substantial indoor air pollution.¹¹ The World Health Organization estimates that more than three billion people still burn wood, dung, coal and other traditional fuels inside their homes¹². The resulting indoor air pollution is responsible for 1.6 million deaths each year, with the majority of them being young children and their mothers. There are also other serious health effects that produce respiratory infections, likely reductions in lung function development in the exposed children, eye irritation, etc.¹³ These low efficiency stoves give off smoke that contains hazardous chemicals.¹⁴ Numerous studies, both epidemiological and physiological, have shown diverse detrimental health effects.¹⁵

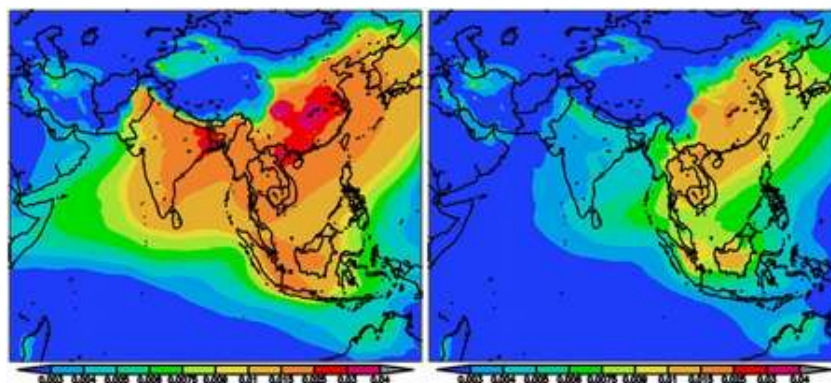


Figure 1: The pollution effects of cooking using biomass (wood, cow dung, ect.) in south Asia: Left, levels of pollution as of 2005. Right, removes the effects of biofuel cooking. *Source:* V. Ramanathan and G. Carmichael, "Global and regional climate changes due to black carbon", *Nature Geoscience* 1, 221-227 (2008).

The emissions from biomass burning produce large quantities of carbon-containing particles, including light absorbing “elemental carbon” or black carbon particles (soot). It is now recognized that these black carbon particles can have a significant impact on global climate.¹⁵ Furthermore, cook stoves are responsible for 75% of the soot generation, while only 25% is due to transportation.¹⁶ As yet, the Intergovernmental Panel on Climate Change (IPCC) has not issued a CO₂ equivalent value for carbon soot, but it should shortly, since soot can be a more significant contributor to global warming than CO₂, especially in equatorial Asia.¹⁷ Even more directly, the accumulations of soot on the surface of glaciers and pack ice accelerate their melting.¹⁸

The people who generate the soot while cooking, and whose health is impaired in the process, are typically the same people who live “off the grid” in rural areas not served by centralized electrical power generation and distribution networks.¹⁹ There are nearly two billion people worldwide without access to electrical power or hydrocarbon fuels. The time they spend to gather biomass cannot be used in other productive work or education, and the lack of electricity also means that refrigeration is unavailable for either preservation of fresh foods or storage of medicines.

Rural agricultural communities in South-East Asia produce significant amounts of corn and rice. The milling and drying of 1,000 kg of rice produces 650-700 kg of white rice and 220 kg of rice husks. A related estimate suggests that the 645 million-ton rice harvest of 2007 generated 129 million tons of rice husks. Those rice husks have an energy content of about 12.5 ± 2.5 MJ/kg.²⁰ In terms of petroleum-based liquid fuels, the energy content of one ton of rice husks is equivalent to the energy contained in 365 liters of gasoline (34.2 MJ/liter) or 378 liters of kerosene (33 MJ/liter). Unfortunately, burning of corn cobs or rice husks in conventional cook stoves tends to make a smoky, unstable fire and leaves a tar-like residue.²¹

The addition of an electrically-powered fan can greatly improve combustion. Recent research on biomass cooking stove improvement has conclusively demonstrated that the use of a fan to force air convection within the combustion chamber provides the greatest benefit in terms of improved indoor air pollution, reduced soot production, and fuel flexibility without increasing cooking time. Using state-of-the-art instrumentation (*e.g.*, FTIR spectroscopy and particulate light scattering) under a laboratory emission hood, the Aprovecho Research Center measured the emissions from six improved cooking stoves.²² As shown in Figures 2 and 3, the performance of the stove that used fan-forced convective combustion performed significantly better in all four categories.

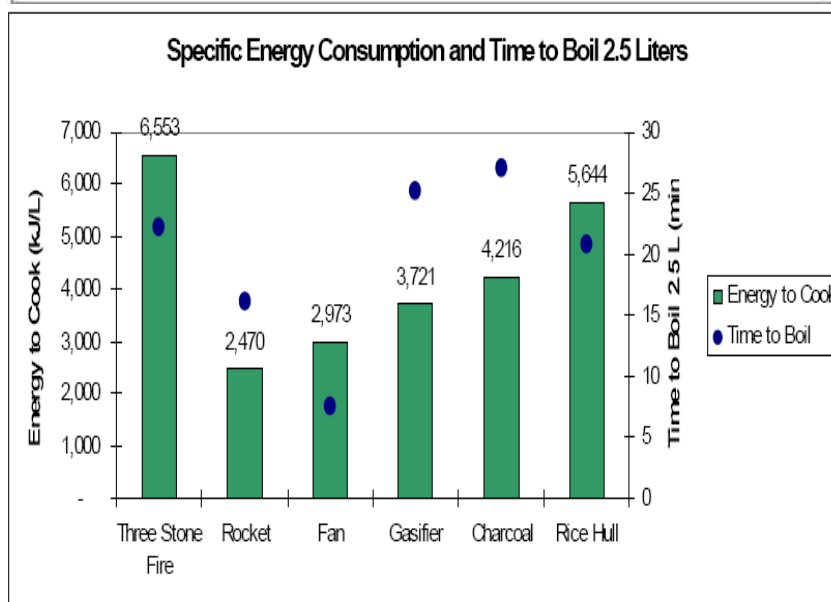
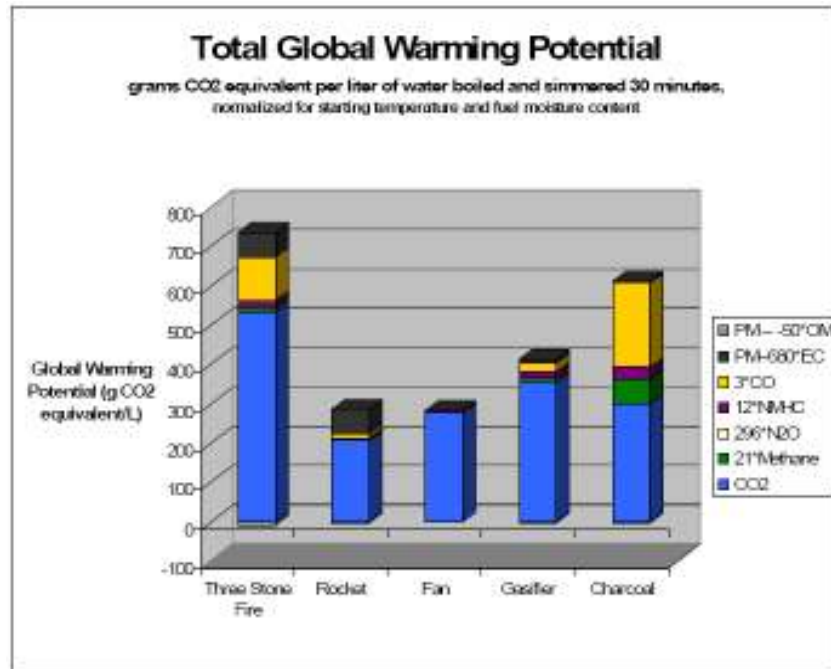


Figure 2: Results of the comparison of different improved cook stove systems showing the reduction in Total GWP (above) and energy consumption (bottom). The value of the fan-forced convective combustion is clearly demonstrated by both figures. *Source:* N. MacCarty, D. Ogle, D. Still, T. Bond, C. Roden and B. Willson, *Laboratory Comparison of the Global-Warming Potential of Six Categories of Biomass Cooking Stoves*, Tech. Report, 26-pages, Aprovecho Research Center, Advanced Studies in Appropriate Technology, Creswell, OR (Sept. 2007).

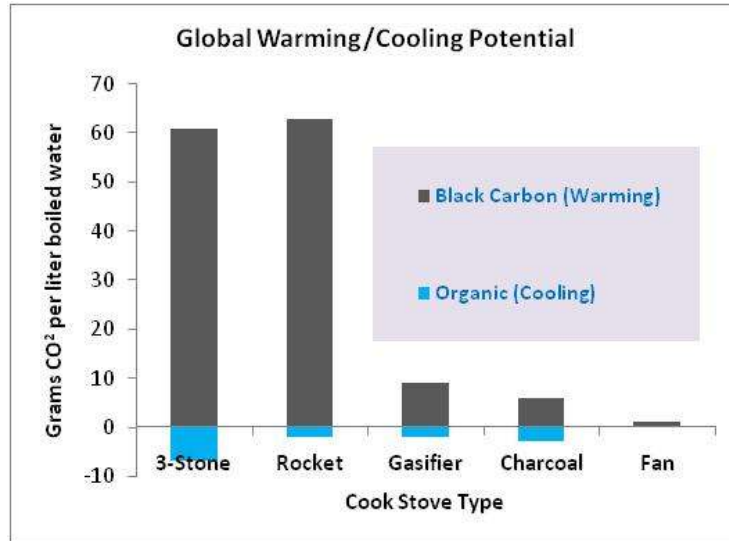


Figure 3: The global warming and cooling potential of particulate matter from the same stoves as Figure 2. Organic carbon creates cooling due to reflection while black carbon (soot) produces warming. The vertical axis shows the number of grams of Carbon dioxide equivalent per liter of water brought to a boil and simmered for 30 minutes. The black carbon (soot) warms the atmosphere and the organic carbon has an atmospheric cooling effect. The fan stove also reduces indoor air pollution as well as cooking time to reach boil. *Source:* N. MacCarty, D. Ogle, D. Still, T. Bond, C. Roden and B. Willson, *Laboratory Comparison of the Global-Warming Potential of Six Categories of Biomass Cooking Stoves*, Tech. Report, 26-pages, Aprovecho Research Center, Advanced Studies in Appropriate Technology, Creswell, OR (Sept. 2007).

Many rural villages around the world do not have electrical service and thus, may not easily be able to take advantage of improved stove technology unless it can be self-powered.

To date, only thermoelectric (TE) modules made by Philips have been used to generate electricity from the waste heat produced by the cook stove itself.²³ In addition to the Philips woodstove prototype, a version of the Envirofit stove has had a thermoelectric module attached,²⁴ and the Mara Sarakham University in Thailand has added a TE module, although it did not use the electricity to power a fan to improve stove performance.³ Clearly, the advantage of a TE module is that is a solid-state device that has no mechanical moving parts and can generate electricity directly from a temperature gradient using the Seebeck effect.²⁵

Like any heat engine, the TE module must exhaust its heat to a lower-temperature reservoir. To create the temperature gradient required for electrical power production, the cold-side junctions are usually connected to a heat sink that can be air-cooled by natural or fan-driven convection.

Unfortunately, the best material currently available for TE modules is bismuth-telluride, which is both brittle and hygroscopic - two properties that are problematic in a kitchen and in the humid environment of equatorial-Asia. Furthermore, the thermal efficiency of a TE module is rarely greater than five percent of the maximum theoretical (Carnot) efficiency η_{Carnot} that is determined only by the hot and cold reservoir absolute (Kelvin) temperatures.

$$\eta_{Carnot} = \frac{T_{hot} - T_{cold}}{T_{hot}}$$

Bismuth-Telluride thermoelectric modules fail if the junctions exceed 200 °C (473 K). Since a practical exhaust temperature is rarely below 47 °C, the resulting Carnot efficiency can never exceed 32 %.

1.2 Objectives

The objective of this thesis project was to develop a simple, inexpensive, and mechanically robust thermoacoustic generator to produce electrical power to determine if a thermoacoustic approach is feasible. That electricity could run a fan to improve the efficiency of a biomass-burning cook stove and provide excess electrical power that can be used for high-efficiency lighting and charging small electrical appliances like mobile telephones. This objective is simplified by the fact that excellent stoves have been developed which use a fan but require an external source of electrical power. In this research, we propose to develop our prototype to extract a small amount of heat from such a stove and use a thermoacoustic engine to produce at least enough electrical power to run the fan.

The long-term objective of this effort is to provide an attractive option to manufacturers of improved cook stoves that use fans to enhance performance. Since the thermoacoustic generator will use only inexpensive and non-toxic components, it should be suitable for appliances that have to be provided to those who have very little disposable income.

The shorter-term objective is to create a thermoacoustic prototype that can convince major corporations and foundations that either produce such appliances or fund the production of cook stoves that such small-scale waste-heat electrical co-generation is both technically and economically feasible.

This effort started by (i) searching for an existing loudspeaker that could be used as the linear alternator and by (ii) optimizing a computer model that would incorporate the loudspeaker as an element in that model. Such a model would also include a “stack” where the thermal-to-acoustic conversion takes place, the resonator components (*i.e.*, the hot duct and the ambient duct which acoustically couples the sound power that exits the ambient heat exchanger to the loudspeaker), and a heat exchanger that removes the waste-heat from the stack and exhausts that heat.

1.3 Design Constraints and Challenges

The challenge that this thesis will address is how to provide electricity to power the fan in the rural villages of the developing regions of South-East Asia, mostly in Burma, Cambodia, Laos and Vietnam, that are typically “off-grid” but have an abundance of combustible agricultural waste, particularly rice husks. Given a heat engine strategy with adequate efficiency, the waste heat generated by the cook stoves could provide electrical power for other uses as well. The goal of this research, therefore, was

the production and testing of a heat-driven thermoacoustic generator prototype that would be affordable and could be manufactured and/or assembled in a developing country.

There are two initial design constraints which make sense. Although most high performance thermoacoustic devices use inert gas (usually helium), at pressures between 10 and 40 atmospheres, to increase volumetric power density and heat transfer efficiency, this design effort will be restricted to using air at atmospheric pressure. This choice will simplify the construction of the resonator and reduce demands on its design which would typically have to be contained entirely within a certified pressure vessel.

The second constraint would be the use of a commercially-available material for the stack. Three types of Celcor™ ceramic shown in Figure 4 were used in experimentation.²⁶ Stainless steel honeycomb was also considered to be a potential stack material. However, due to its high thermal conductivity compared to ceramic, it was not employed in this.

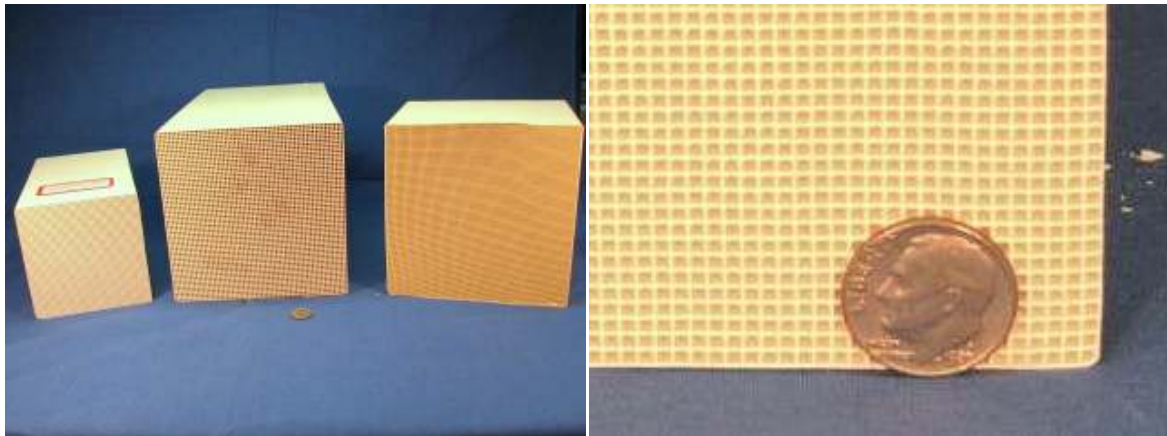


Figure 4: (Left) 100, 200, and 400 cells/in² ceramic stack material. (Right) Close-up photo of the 200 cell/in² stack material.

Celcor™ has been used in a number of thermoacoustic devices because it is inexpensive and is readily available. It is employed worldwide as a substrate for the platinum catalyst placed in the muffler that is used to reduce automotive tailpipe emissions.

The more challenging heat exchanger design will be at the hot end where the heat from the stove enters the thermoacoustic generator. At those temperatures, both material choices and thermal radiative transport need to be considered.

1.4 Basic Thermoacoustic Theory

To convert waste heat created from the biomass-burning cook stove to an acoustic signal that can be harnessed by the linear alternator, there needs to be a temperature difference across the stack material great enough to cause the resonator to go into onset. Onset meaning that the system becomes a “self-

maintained oscillator” that produces a standing wave oscillation of the air within the resonator without the aid of any mechanical parts.²⁷

The easiest way to understand a thermoacoustic engine at onset is to visualize a small “parcel” of air within one of the stack cells. This cycle begins with the air parcel is driven to the hot side of the stack by a low pressure caused by the final step of the cycle. Because the air parcel is now surrounded by stack material hotter than it so heat is conducted out of the stack and into the parcel. The air is heated even further due to the pressure increase, as the end of the hot duct is rigid and impenetrable. This would happen at a fast enough rate so that the heat has a limited time to flow out of the air. The high-pressure, high-temperature parcel is driven away from the hot side of the stack by its own thermal expansion. The air parcel now moves towards the other side of the stack where it is surrounded by stack material much cooler than it. Heat is conducted out of the air, into the walls of the stack. The parcel of air is further cooled by a thermal expansion of the gas in low pressure environment. This cool air parcel is forced back to the hot end of the stack due to the low pressure where this cycle starts over again.⁶ An illustration of this process can be seen in Figure 5. A simple example of a thermoacoustic device can be seen in Figure 6.²⁸

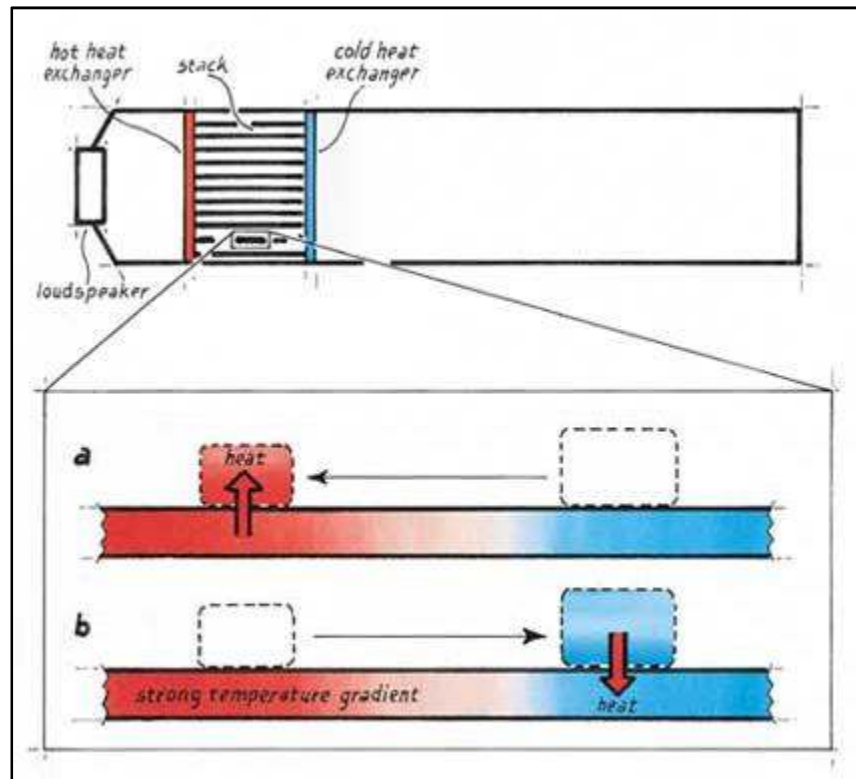


Figure 5: Schematic showing the heat transfer between the air and the stack material. *Source:* S.L. Garrett and S. Backhaus, “The Power of Sound”, *American Scientist*, pp 516-525 (2000).

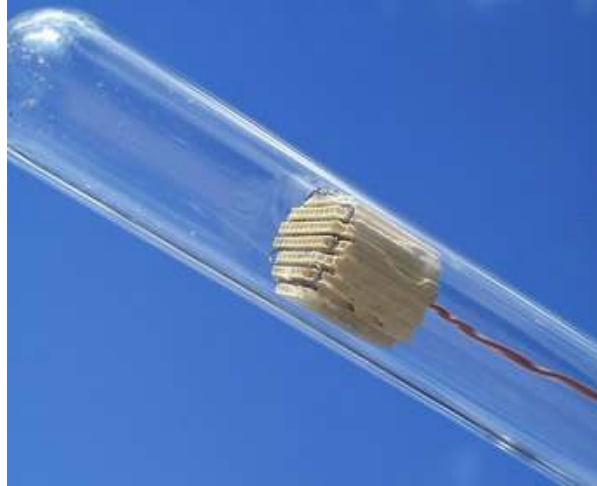


Figure 6: This photograph shows a simple thermoacoustic engine demonstration device that has been made available in kit form since 2000. In this simple device, a test tube is the acoustic resonator and the thermoacoustic “stack” is Celcor™ ceramic with a cell density of 400 cells/in². A serpentine NiCr heater wire can be seen which heats one end of the stack. Since the end of the test tube which is not visible in the photo is open, forced air convection, driven by acoustical streaming, cools the other end of the stack by convection so an ambient temperature (exhaust) heat exchanger is not required. *Source:* S. L. Garrett and R-L. Chen, “Build an ‘Acoustic Laser’”, *Echoes* **10**(3), 4-5 (2000).

With the air oscillating at a wavelength much greater than the physical length of the resonator body, the compressibility of the air within the resonator can be assumed to be a lumped-element. This acoustic signal can be converted to an electrical power using any electroacoustic transducer. In the case of this thesis project, two inexpensive 4-inch loudspeakers were used.

CHAPTER 2

ENGINE DESIGN AND BUILDING PROCESS

Ordinarily when attempting to optimize power density, most thermoacoustic devices are designed to work at the highest practical mean pressures, usually using helium gas as the thermodynamic working fluid. Since our goal was to develop an inexpensive device, we decided that the thermodynamic working fluid would simply be air at ambient pressure. This choice allowed us to abandon the traditional cylindrical resonator shape that is required to contain pressurized gas with a minimum resonator wall thickness and use instead a relatively thin sheet metal resonator hot duct and make the overall resonator cross-section rectangular. With a rectangular resonator, we could use an ordinary finned heat exchanger,²⁹ similar to those used to cool electronic components (*e.g.*, power transistors, microprocessor chips), instead of the fluid-filled heat exchangers, similar to automobile radiators, to remove waste heat from the ambient-temperature end of the stack.

This design is also different from earlier thermoacoustic engine designs as it does not use a standing-wave resonator. Instead, the resonance frequency is determined by a lumped-element combination of the gas stiffness, provided by the air in the hot and ambient ducts, and the physical mass of the loudspeaker and balsa-wood “plunger” bonded to the speaker’s cone. The exchange of the kinetic energy of the moving speaker components (*i.e.*, voicecoil and cone) and the plunger, with the potential energy stored by the compressibility of the gas within the resonator act as the “flywheel” for our engine. By using physical mass in this configuration, rather than the gas mass in a more conventional standing wave resonator,³⁰ we hope to avoid both linear viscous losses and the potentially more dissipative nonlinear mechanisms (*e.g.*, turbulence and “minor loss”).³¹

2.1 Mock-Stove

We have constructed an entire, fully-instrumented, half-engine (hot-duct, stack, ambient-temperature heat exchanger, cold-duct, and linear alternator) before attempting a dual-stack differential (push-pull) engine that would be incorporated into a stove. To evaluate both the radiative heat transfer and the operation of the half-engine, it is necessary to provide a controllable heat source that is insulated from the laboratory, both for safety and to allow quantification of total heat flow. To accomplish this goal, a custom furnace was fabricated.

The furnace is constructed from commercially available refractory firebrick³² and assembled with mortar and lined with flexible silica insulation. The firebrick forms the four walls of the furnace as shown in Figure 7. A custom heater was wound in a Celcor™ ceramic holder, using a serpentine NiCr ribbon (0.25” x 0.003”).³³ The heater was mounted on a brick and fits into one end of the furnace to provide the heat source. The other end of the furnace is open to allow the stack to protrude and join with the cold-duct that contains the ambient-temperature heat exchanger and the linear alternator (loudspeaker). To control the temperature of the heater, the current going into the NiCr ribbon was controlled manually using a Variac autotransformer. To limit the degradation of the NiCr ribbon due to oxidation at high temperatures and to improve heat transfer to the hot-end of the hot duct, helium will be blown in to the mock-stove while experimentation is taking place.



Figure 7: (Left) The test furnace is assembled from refractory fire brick that has been cut using a diamond-edge band saw in our laboratory. The brick is then assembled using a refractory mortar. Several mortar seams (dark grey) are visible in the photo. Two bolts have been embedded in the side walls of the furnace to secure the heater element to the end of the furnace. (Right) This is a photograph taken during construction of the electrical heater element that is “woven” into a Celcor™ ceramic substrate that has been grooved to keep the NiCr winding from shorting against each other. The ribbon is about 2 meters in overall length and has an electrical resistance of 4.5 Ω . The heater element has the same area as the duct formed within the test furnace.

2.2 Initial Modeling

The physical values of design choices (*e.g.*, total speaker moving mass, duct length, stack length, heat exchange fin area and length) were optimized initially using the DELTAEC thermoacoustic software developed by the Los Alamos National Laboratory. As parts of the engine were initially optimized in DELTAEC, a computational draft was simultaneously updated using SolidWorks™ to ensure that the manufacturing process would run smoothly. SolidWorks™ is a three-dimensional computer-aided design program. As parts were manufactured or purchased (*e.g.*, heat exchanger, loudspeaker), the DELTAEC and SolidWorks™ models were updated once again and the remaining controlling parameters were changed to determine new optimized values. The initial DELTAEC model can be seen in Appendix A of this thesis.

DELTAEC would be used throughout this thesis project due to its compatibility with each of the different aspects of experimentation. A SolidWorks™ drawing of the thermoacoustic device as built can be seen in Figure 8.

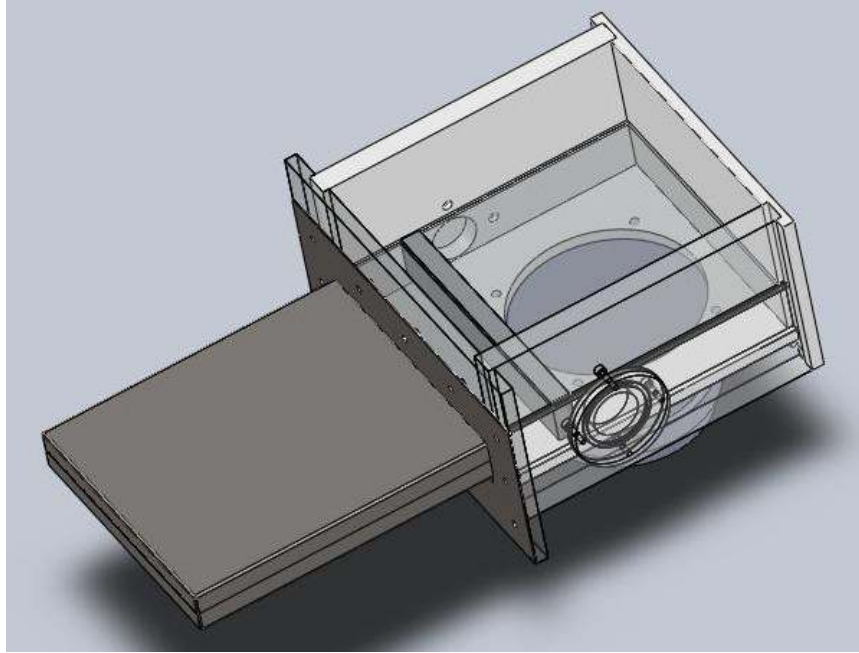


Figure 8: SolidWorks™ model of the assembled thermoacoustic co-generator with the dark grey portion representing the hot duct on the left. Visible through the transparent walls are the finned heat exchanger (also dark grey). Both instrumentation ports are visible. The nearer port is closed with a transparent cap and the farther is open. The ambient duct is on the right with an ice bath adjacent to the top.

2.3 Hot-Side Duct

The hot-duct was made from stainless steel to tolerate the high stove temperatures (in excess of 700 °C). Stainless steel also minimizes the parallel thermal conduction path provided by the duct, which contains the ceramic stack that needs to maintain the temperature gradient necessary to sustain thermoacoustic oscillations. The stainless steel should be as thin as possible both to reduce the nuisance heat conduction along the stack and to reduce the hot-duct heat capacity so that it will come to its operating temperature as quickly as possible.

Of course, the duct material must be thick enough that it will appear acoustically rigid to reduce radiated sound levels and to minimize acoustical losses that would reduce the amplitude of the thermoacoustically-induced standing wave. The minimum thickness was determined by requiring that the lowest vibrational mode of the largest area segment of the duct (16.5 cm x 14 cm) have a resonance frequency above the engine operating frequency. Stainless steel alloy 304, with thickness 0.025" (635 μm) was considerably thicker than required by the vibrational constraint but was easier to weld than thinner sheets and still did not conduct too much heat (< 10 W) from an assumed stove temperature, $T_{hot} = 800$ °C, to room temperature.

A three-piece design (top, bottom, and flange) was drawn up in SolidWorks™, utilizing the sheet metal software add-on. All three pieces were cut using a numerically-controlled water jet and bent into shape using a sheet metal box brake. The final hot duct design has internal dimensions of approximately 140 mm x 160 mm x 26 mm. Due to the instability of using the Metal Inert Gas (MIG) welder to butt-weld

the ends of the hot duct pieces together, which was our initial course of action, a Tungsten Inert Gas (TIG) welder was ultimately used. The welded hot duct is shown in Figure 9. To test the duct for leakage, an air tight aluminum cap with a gas inlet tube was fabricated along with a matching gasket. The duct was pressurized using a helium tank and soapy water was applied along all of the welds. This test confirmed minimal leakage and Devcon™ Aluminum-Filled Epoxy #10710³⁴ was used to cover the areas of the flange where the leaking was occurring.

Due to inherit thermal expansion, and thus permanent warping of the hot duct flange during the welding process, an aluminum backing plate was fabricated, also using the water jet. A rubber gasket was cut that would seal the flange of the hot duct and the aluminum flange of the ambient temperature duct to ensure an air-tight fit. The temperature at the interface is limited by the water in the “swimming pool” that collects and measures the waste heat rejected to the ambient-temperature duct. The stainless steel duct, flange, and gasket are shown in Figure 10.



Figure 9: Photograph of the weld joining the three pieces that form the alloy 304 stainless steel hot duct. An aluminum epoxy³⁴ was applied along part of the weld to prevent leakage (not pictured).

Upon completing the fabrication of the hot duct, the 10 cm long Celcor™ stack was cut to fit into the hot duct. The stack was carefully shaped by hand to produce a close fit to the inner surface of the hot duct. Figure 10 shows the Celcor™ stack inside the hot duct. Part of the stack protrudes from the duct by 3 cm to enter ambient temperature duct and make contact with the ambient-temperature heat exchanger fins. Different lengths of stack material were used throughout experimentation.



Figure 10: Left to Right – Rubber gasket, aluminum backing plate, and hot duct containing the Celcor™ stack.

2.4 Ambient Temperature Duct

The ambient duct has three functions: One is to complete the lumped-element acoustic resonator by providing a transition from the hot duct while housing the loudspeaker that will function as the linear alternator to generate electricity from the thermoacoustically-driven pressure oscillations. The second function is to contain the ambient-temperature heat exchanger that removes the cook stove waste heat from the stack. The third function is as an ice bath that collects the waste heat from the heat exchanger. In addition to removing the waste heat, the ice plays an extremely important role in measurement of the heat flow. In combination with the measured electrical power generation, it determines the overall efficiency of the thermal-to-electrical energy conversion. Since both the mass m of the ice and its enthalpy of melting are known, measurement of the time-rate-of-change of the ice's melting determines the rate of heat flow \dot{Q} through the engine.

The design for the ambient temperature duct was also created in SolidWorks™. Both aluminum and polyvinyl carbonate (PVC – Type 1) were used in the assembly due to their structural rigidity, easy machinability, and good thermal insulation properties. Aluminum was used where heat transfer was encouraged, and PVC acts as an insulator. All pieces of the duct were cut on the numerically-controlled water jet and “slotted” afterward using an end mill.

To minimize leakage that would reduce the acoustic amplitude or allow water to enter the resonator, the walls of the duct were grooved so they could be slid into place. The bottom, two sides, and aluminum flange were fit together and permanently joined using Devcon™ Aluminum-Filled Epoxy #10710³⁴. A photograph of that assembly, viewed from the aluminum flange that joins the hot-duct flange, is shown in Figure 11. Twelve 6-32 machine screws are used to join the ambient temperature duct's aluminum face-plate to the hot-duct flange. Those twelve screws were tapped into the aluminum flange and permanently secured using the same epoxy.



Figure 11: Flange, sides, and bottom wall of the ambient-temperature duct are grooved and bonded using an aluminum-filled epoxy. Also visible in this view is one of two instrumentation ports held in place by four screws that are sealed to the wall with epoxy. Not visible on the instrumentation port is the 2-026 O-ring that provides the gas-tight seal between the instrumentation flange and the ambient duct. The sensors (*e.g.*, microphone and thermocouple feed-throughs) have not yet been inserted in the port cap. Further detailed photos of the instrumentation ports are shown in Figure 13.

The remaining walls of the duct (back and upper wall) fit together with the grooved slots but were not joined using epoxy. Because it will be desirable to interchange parts of the duct, paraffin wax was used as a bonding agent for these two components. A test piece was first used to determine if the wax would bond PVC to aluminum. This was done by heating the aluminum and PVC to 65 °C in an oven, then pouring melted wax (also at 65 °C) along the joining slots of the walls. It was found that this was an excellent way to create a re-sealable bond for those removable walls of the duct while keeping the structure rigid and both water-tight and air-tight. To guarantee a non-leaking ice bath, this area of the ambient temperature duct was lined with a Vinyl Epoxy.³⁵

A wedge was made to displace volume within the ambient temperature duct. This will decrease the acoustical compliance of the air inside the ducts by excluding some compressible volume within the ambient-temperature duct. This results in an increased operating frequency and increased efficiency of the system. This wedge will also direct the warm air leaving the stack closer to the upper aluminum wall, aiding in heat transfer out of the system and into the water bath. The wedge is made of 3/4 inch thick PVC which was initially cut on the water jet and then cut once more on the vertical band-saw. This band-saw cut created a 30-degree angled front wall of the wedge to direct the flow of the oscillating air that is driving the loudspeaker, and thus reduces the flow losses of the fluid's motion. The wedge has two tapped 6-32 screw holes where it is joined to the resonator's bottom wall. The 90 mm diameter hole is concentric with the balsa "plunger" extension of the driver's cone.

2.5 Heat Exchanger

A finned heat exchanger that was cut from an Intel BXSPS100P Xenon® Processor 5500 Series high-performance (passive) heat sink using an electronic discharge (*i.e.*, spark erosion) machine. The fins are placed directly adjacent to the end of the Celcor™ stack within the volume of ambient-temperature duct. The 1.0 cm x 2.1 cm x 13.5 cm heat exchanger is has a fin density of 20.4 fins/inch. The aluminum fins are 225 μm thick and 21 mm long and are bonded to a 5.0 mm thick copper base.

The “characteristic length” of one fin is $\lambda = 17$ mm. Since the fin length $h = 21$ mm, the fin efficiency, $\eta_{fin} = 71\%$.³⁶

$$\lambda = \left[\frac{\kappa_{Al} A}{h_{\infty} P} \right]^{1/2} \cong \left[\frac{\kappa_{Al} t}{2h_{\infty}} \right]^{1/2}; \quad \eta_{fin} = \frac{\tanh(h / \lambda)}{(h / \lambda)}$$

Those results assume $\kappa_{Al} = 240$ W/m-K,²⁹ the convective heat transfer coefficient of air under acoustic conditions $h_{\infty} \cong \kappa_{air} / \delta_{\kappa} = 92$ W/m²-K, and the fin’s area-to-perimeter ratio $A/P \cong t/2$. As seen in Fig. 12 (Right), the finned heat exchanger fits into the upper wall of the ambient duct and is secured using the Devcon aluminum-filled epoxy.³⁵

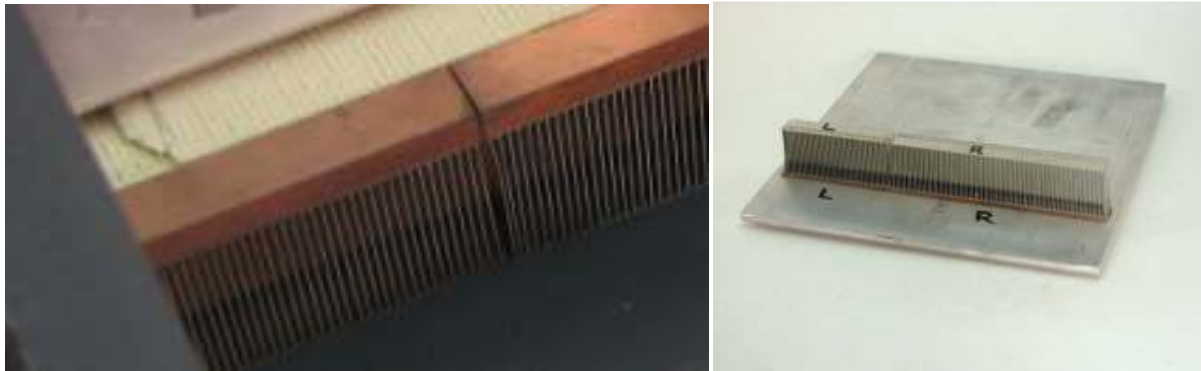


Figure 12: (Left) Close-up photograph of the finned heat exchanger in contact with the ambient-temperature end of the stack that protrudes from the hot duct before the fins were joined to the top of the ambient duct. (Right) The heat exchanger fins shown in the upper aluminum wall of the ambient duct prior to being joined to the wall along the copper base with epoxy.

2.6 Instrument Portals

To provide access into the duct for thermocouple leads and a microphone, two circular, 24 mm diameter portals were cut into the sides of the duct to provide access in the space between the heat exchanger and the wedge. Caps for these two portals were cut on the water jet. Size 2-026 O-rings were fitted onto these caps between the opening of the duct and the screws to ensure an air-tight seal using an O-ring tool in a lathe to cut the manufacturer’s specified groove dimensions.³⁷ One instrument cap contained a piezo-resistive microphone³⁸ and manually controlled pressure release valve. This valve was necessary due to the thermal expansion of the air within the resonator causing possible irreversible damage to the linear alternator. A second instrument portal was used for four E-type thermocouples. A

thermocouple used to measure the air within the resonator was simply built into and epoxied to the cap, where as the three other thermocouples traveled through the cap using gold pins. The caps and ports are shown in Figure 13.



Figure 13: Pictures of each instrument portal caps made from 1/8 inch thick Type-1 PVC. Both are screwed onto the resonator using four 8-32 screws. There is a size 2-026 O-ring that sits in a grooved depression. Left: The piezo-resistive microphone was tapped into the PVC. A hose barb was used as a pressure release valve using the device laying directly to the left of the cap. Right: This portal cap has four thermocouples fastened into it. A thermocouple that reads the internal air of the resonator, and three more thermocouples used for measuring stack temperatures. Gold pins are used to provide a demountable means for making electrical connections between the thermocouples inside the resonator to the instrumentation outside the resonator.

2.7 Linear Alternators

A survey of existing readily-available 4" (nominal) moving-coil electrodynamic loudspeakers was done primarily *via* the Parts Express website.³⁹ The results of that study are summarized in Appendix B.

After comparing the important mechanical and electrical properties (as well as price), the Dayton DA115-8 and ND105-4 were chosen as the two best compromises for the initial prototype tests (see Figure 14). Two Dayton DA115-8 and four ND105-4 were purchased and tested to determine the electro-mechanical parameters, (*i.e.*, moving mass, mechanical compliance and resistance, electrical resistance and inductance, $B\ell$ -product, and resonance frequency) to be used in the calculations and DELTAEC models (see Table 1). The manufacturer's specifications of the two drivers used are provided in Appendix C.

		Dayton 115-8				Dayton ND105-4			
		#3	#4	#5	#6	#1	#2	#3	#4
Res Freq	Hz	61.35	65.10	61.31	63.08	66.63	66.62	67.97	64.55
R_{DC}	Ω	6.364	6.389	6.466	6.381	4.067	4.060	4.092	4.130
R_{MS}	kg/sec	1.129	1.169	1.185	1.034	0.523	0.541	0.499	0.711
Stiffness	N/m	984	1,068	989	994	1,240	1,247	1,261	1,193
M_o	gram	6.44	6.27	6.44	6.05	7.09	7.02	6.85	6.72
Q	-	2.200	2.193	2.092	2.319	5.673	5.432	5.864	3.832
Bl	N/A	5.599	5.524	5.523	5.888	9.484	9.023	9.751	7.930

Table 1: Results of parameter measurements on four Dayton 115-8 and four Dayton ND105-4 4" (nominal) electrodynamic loudspeakers. Excluding ND105-4 sample #4, the average values of $R_m = 0.52$ kg/sec is less than half that for the 115-8 ($R_m = 1.13$ kg/sec) and the ND105-4 has an average value of the Bl -product ($Bl = 9.4$ N/A) that is 50% larger than the Dayton 115-8. The prices of those two models are the same (approximately 11.00 USD/each). The manufacturer's value for the effective speaker cone area S_D is 53.1 cm² for the 115-8 and 51.5 cm² for the ND105-4.



Figure 14: Left: Dayton DA115-8 4 inch loud speaker. Right: Dayton ND105-4 4 inch loudspeaker.

To displace volume, as well as add mechanical mass to the driver, a Balsa wood “plunger” was fabricated on a lathe and joined to the cone of the Dayton DA115-8 using the same epoxy used in the fabrication of the ambient temperature duct walls. The alternator-plunger device can be seen in Figure 15. A ¼-20 bolt was placed through the center of plunger to allow for the variation of mass to the linear alternator by adding or removing hex nuts (see Figure 15). This made it possible to tune the response of the linear alternator without substituting different drivers to change the desired frequency and quality factor, Q .



Figure 15: Dayton DA115-8 4" linear alternator with the balsa plunger joined to the cone.

The driver is joined to the bottom plate of the resonator using four 8-32 machine screws captured in the lower duct wall. A cork gasket was used to provide an air-tight seal. The positioning of the speaker was designed so that the plunger goes up into the ambient temperature duct, through the hole in the wedge.

2.8 Entire Assembly

The entire, finished assembly can be seen in Figure 16, along side of the initial SolidWorks™ computational drawing.

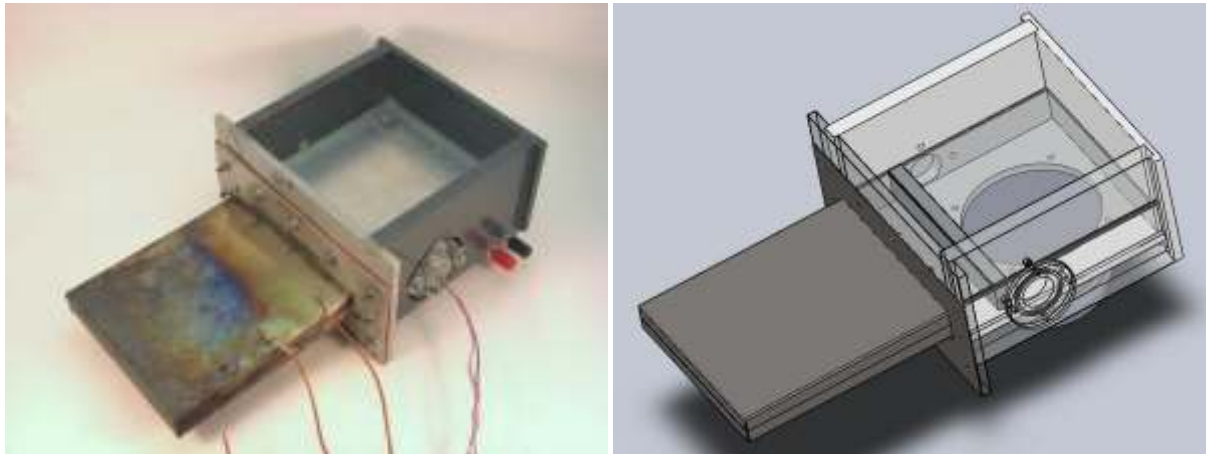


Figure 16: Thermoacoustic engine assembly pictured next to SolidWorks™ model. Apparatus measures approximately 25 cm long. The upper wall of the SolidWorks model was made transparent to show the inside of the Ambient Temperature Duct.

CHAPTER 3 EXPERIMENTAL METHODS

The experimental setup of the thermoacoustic device had to be simple and fit onto a lab bench (see Figures 19 and 20). This proved to be challenging due to the large amounts of data being taken for individual tests. Initial measurements were performed to calculate radiant heat deposited on the hot side of the stack and heat transfer out of the device (Chapter 4). This had to be done to determine if radiant heat transfer from the hot-end of the resonator to the hot end of the stack was sufficient to provide a substantial temperature gradient across the stack. If not, a second heat exchanger will be required in the resonator next to the hot side of the stack.

Once heat transfer testing was completed, the device's performance was tested in "Helmholtz mode" using a tube to substitute for the loudspeaker (Chapter 5) and power extraction mode (Chapter 6). Heat transfer was still examined during these processes. For both sets of tests, the dampening factors which limited the resonator from going into "onset" were examined. This required the use of pressure and voltage measurement instrumentation. After the device reaches onset, the performance of the resonator was monitored. In the Helmholtz mode, this was done by measuring the sound pressure within the resonator. In this power extraction mode, this was done by measuring the loudspeaker output voltage across a variable load resistance.

3.1 Testing Instrumentation

An HP 34970A Data Acquisition/Switch Unit (DAQ) is a versatile and highly accurate measurement system that can be configured to measure either alternating current (AC) or direct current (DC) and voltages, 2-wire or 4-wire resistances, and frequencies. It has internal calibrations and cold-junction compensation to convert thermocouple voltages to temperatures and thermistor resistances to temperatures. The unit used in this experimentation has a 20-channel multiplexer card installed that is programmed to acquire signals from seven E-type thermocouples and a thermistor,⁴⁰ and measure two currents and two voltages that characterize the performance of the co-generator and measure the electrical power dissipated by the furnace's heater. The channel list is provided in Table 2 below:

Channel	Sensor	Function/Location	Wiring
1	AC Voltage	Microphone output	Red/Black
2	TC2	Hot-duct rear (heater)	Type-E
3	TC3	Hot-duct middle	Type-E
4	TC4	Hot-duct front	Type-E
5	TC5	Stack (hot end) - Center	Type-E
6	TC6	Stack (hot end) - Corner	Type-E
7	TC7	Stack (ambient end)	Type-E
8	TC8	Resonator gas (ambient)	Type-E
9	Thermistor	Water bath	Green/White
10	AC Voltage	Variac™	Grn-Wht/Brn-Blk
11	AC Voltage	Variac™ 0.1 Ω current sense	Blue/Grey
12	-	-	White/Green
13	DC Voltage	Microphone Output	Purple/Green
14	Frequency	Linear alternator output	White/Brown
15			
16			
17			
18			
19	Thermistor	4-wire Ω sense	Red/Black
20	AC Volts	Linear alternator output	Red/Green
21	AC Current	Linear alternator output	Black/White
22			
Alarm #1	Thermistor	$T_{water} > 60\text{ }^{\circ}\text{F}$	
Alarm #2	DC Mic Out	$ V_{DC} > 100\text{ mV}$	

Table 2: Channel list for the multiplexed HP 34970A Data Acquisition and Switch Unit with model 34970A 20-channel multiplex card. In addition to 20 channels for voltage, resistance, temperature, and frequency measurements, there are two additional channels dedicated to current measurement ($I \leq 3.0\text{ A}$) and four alarm/digital outputs.

LabVIEW 2009 Student Edition was used to take readings from the DAQ system and onto a notebook computer every thirty seconds throughout experimentation, *via* GP-IB cable (IEEE 488). These readings were recorded to a spreadsheet that could be analyzed after the completion of the experiment using Microsoft Excel. The LabVIEW user interface and monitoring system are shown in Figures 17 and 18.

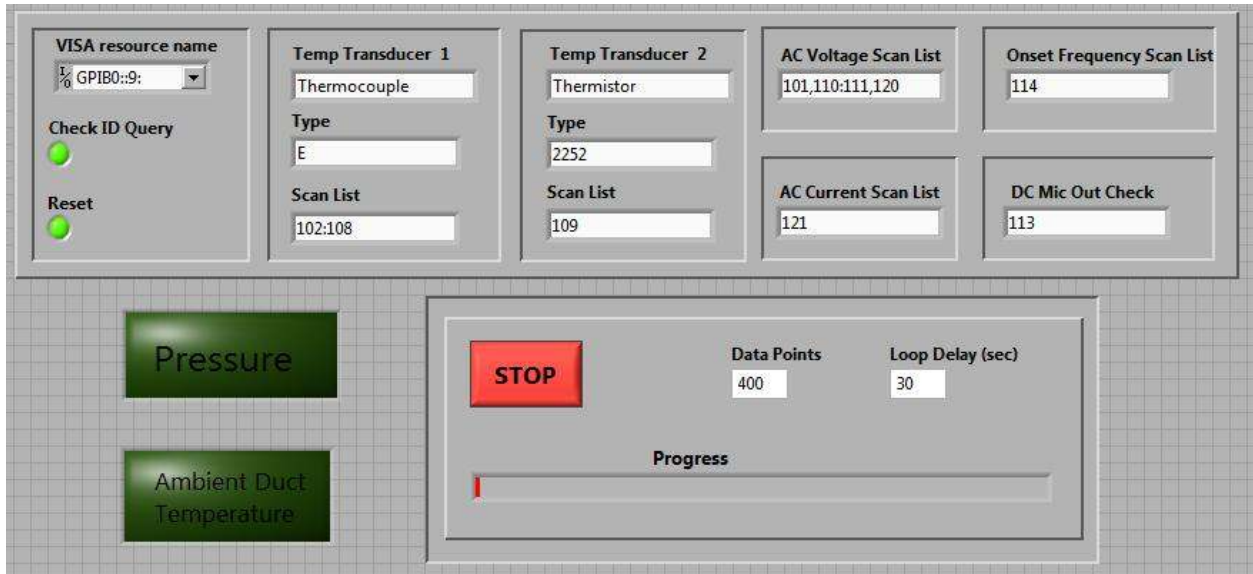


Figure 17: LabVIEW 2009 Student Edition user input interface for experimentation. Scan lists correspond to the terminals of the data acquisition system’s 20-channel multiplexed input card (HP 34901A) used to wire the sensors into the HP 34970A Data Acquisition Unit. This screenshot includes two green warning lights (bottom left): one for the internal pressure of the resonator and the other for the temperature of the ambient duct water bath.

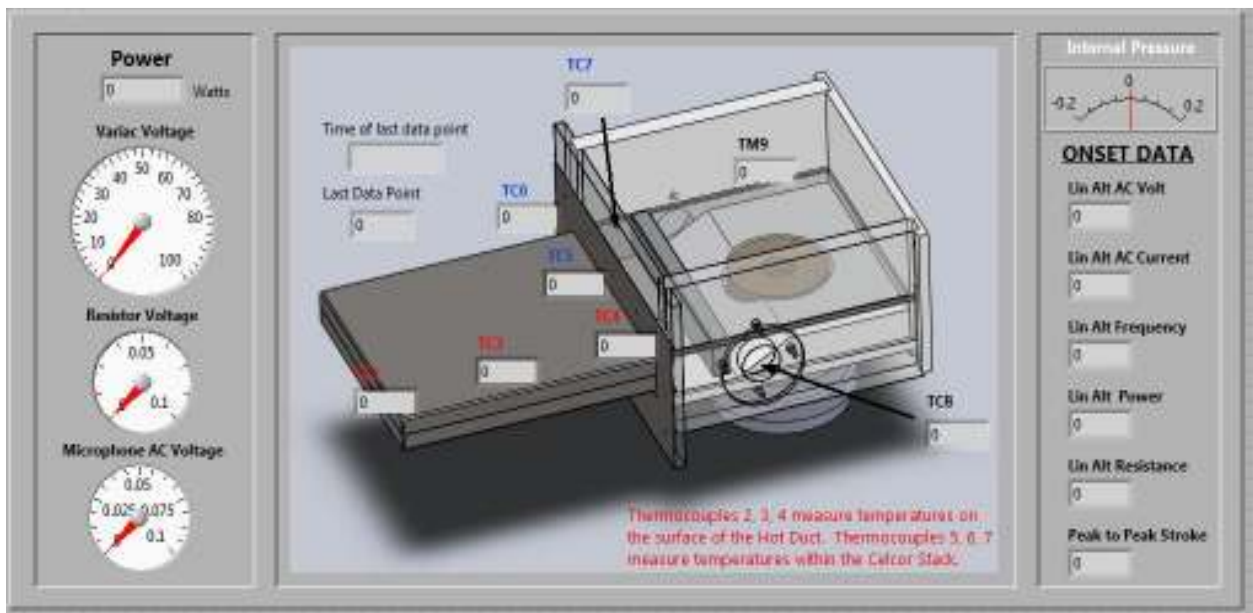


Figure 18: Screenshot of the LabVIEW 2009 Student Edition user’s experimentation monitoring system. Left: Variac power and internal microphone data. Center: SolidWorks drawing of resonator labeled with corresponding thermocouples and thermistor values with the time of the last reading along with the current data point logging number. Right: Internal pressure monitor including the internal microphone output voltage and important linear alternator (loudspeaker) data.

For all experiments (pre-/post- onset, Helmholtz Resonator/Engine), LabVIEW recordings were taken simultaneously with other measurements described in greater detail in their respective chapters in this thesis.

3.2 Laboratory Bench Setup

Figure 19 shows the thermoacoustic device ready for experimentation. The hot side duct is placed in the mock stove. The insulation seen on top of the ambient temperatures side of the engine is used to limit heat transfer into the ice bath. An ice bath thermistor⁴⁰ can be seen going vertically through the insulation. Figure 20 shows the entire configuration of the apparatus and instrumentation for the computer-controlled measurement of the properties of the thermoacoustic engine.

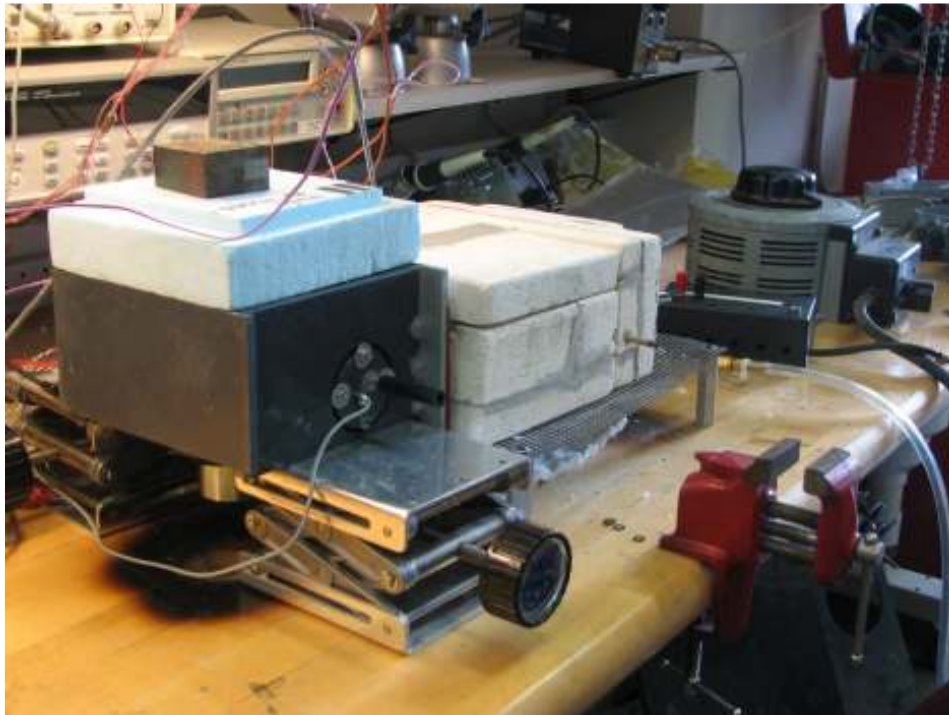


Figure 19: Lab bench setup for experimentation on the thermoacoustic engine. Near: Ambient side of the engine propped up with two lab-jacks. Middle: Mock-stove engulfing the hot side duct. Far: Variac with custom built resistor housing wired in series. The resistor was used to measure the power output of the Variac going into the NiCr ribbon³³ used as a heater within the mock-stove.



Figure 20: Overview of entire lab bench setup while testing was in progress. The data acquisition (laptop) computer is visible at the left. In the right foreground is a cylinder of compressed helium gas that provides a steady stream of gas to improve heat transfer to the hot duct and reduce the oxidation of the NiCr heater element.

CHAPTER 4 HEAT TRANSFER DATA

The heat transfer properties of the resonator were investigated to determine if a second heat exchanger on the hot-side of the stack was necessary to get the stack temperature difference large enough for the device to go into onset. This two-heat exchanger design is typical of many thermoacoustic devices. With the absence of a hot-side heat exchanger, resonator design can be simplified and the material costs will be lowered. Temperature readings were taken while a test was in progress with the thermoacoustic device set up as described in Chapter 3.

Three E-type thermocouples were equally-spaced along the outside of the hot duct going from the very end of the resonator adjacent to the electrical heater element, up to the flange where the hot duct is bolted to the ambient temperature duct's 1/8" thick aluminum flange (TC 2, TC 3, TC 4, respectively). Three more E-type thermocouples were placed internally within the resonator, on the Celcor stack. Two were placed on the hot side of the stack (TC 4, TC 5), and one on the cold side of the stack (TC 6). Since both hot-side thermocouples typically agreed to within ± 10 °C, the average of the hot side temperature readings were used in the remainder of this report.

The LabVIEW measurements were done in conjunction with the acoustic resonance decay measurements presented later on in this thesis (Sections 5.1 and 6.1). The hot side of the stack was heated in the custom electrically-heated furnace using the mock-clay stove. The furnace temperature was controlled using an autotransformer. These temperature readings were used to analyze radiant heat transfer and conductive heat transfer rates. A typical temperature vs. time history is shown in Figure 21.

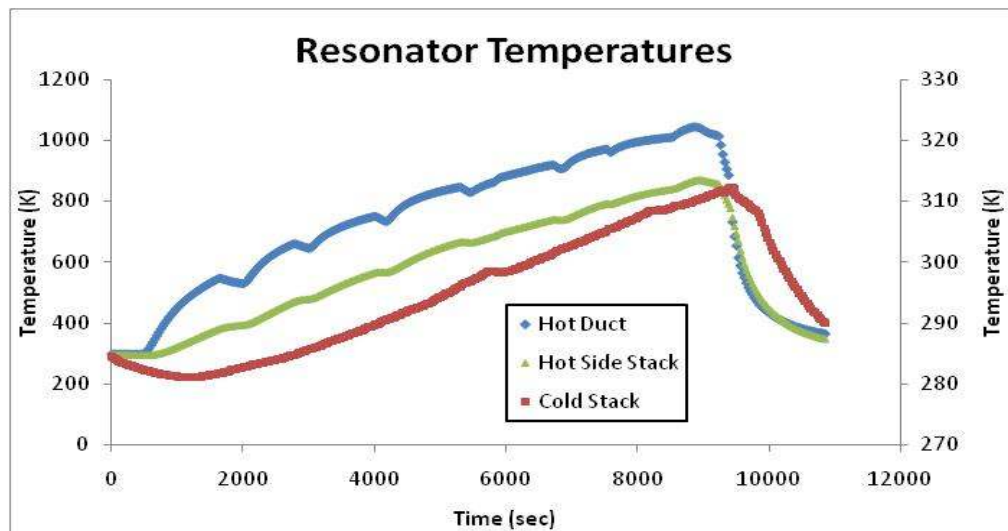


Figure 21: Time dependent temperature readings at critical locations outside (duct) and inside (stack) the resonator. The back wall of the hot duct (blue) and the hot side of the Celcor stack (green) temperature values are read with the left side y-axis. The cold side of the Celcor stack (red) is read with the right side y-axis. All temperatures are displayed in degrees Kelvin.

Distilled water was frozen into blocks of ice weighing about 0.5 kg that were placed in the ambient temperature duct's water bath. The mass of the ice at various times was recorded to calculate the amount of heat transfer going out of the resonator. Often, multiple blocks of ice were used in each experiment.

The raw temperature data recorded by LabVIEW 2009 Student Edition was used to calculate the heat transfer properties of the resonator. All heat transfer equations were plotted using Microsoft Excel. The total simplified heat transfer equation sums the heat transported by conduction q_{cond} with the heat that was absorbed by the latent heat of the melting ice q_{LH} .

$$q_{rad} = q_{cond} + q_{LH}$$

4.1 Assumptions

To further understand the heat transfer process involved within the resonator, six E-type thermocouples were analyzed along with the latent heat data taken from mass measurements of ice melted by the ambient temperature duct ice bath. Several assumptions were made to simplify the analysis of a complex set of equations:

- The rate of radiant heat transfer is assumed to only be dependent upon the materials emissivity/absorption, temperature, shape factor, and area.
- Conduction from the walls of the hot duct to the hot side of the Celcor stack is negligible when compared to the radiant heat transfer.
- All heat transfer flowing out of the resonator enters the ambient temperature duct water/ice bath.
- Heat going into the ice bath only resulted in latent heat transfer (the ice melting), which is equivalent to assuming that the temperature of the bath remained fairly constant.

4.2 Radiant Heat Transfer

The equation used for radiant heat transfer is provided below:⁴¹

$$q_{rad} = \sigma AF(\varepsilon T_{hot}^4 - \alpha T_{cold}^4)$$

σ is the Stefan-Boltzmann constant [$5.67 \times 10^{-8} \text{ W/m}^2\text{-K}^4$], A is the area of exposure, F is the dimensionless shape factor of the material, ε and α are the dimensionless emissivity and absorption values of the material, and T is the absolute (Kelvin) temperature of the materials. The area and temperatures were known from the device's geometry and temperature recordings of the hot-ends of the duct and the Celcor stack. The total radiant heat transfer to the Celcor stack was split into five parts for the five walls of the hot duct (each having its own equation); the back wall, the upper and lower walls, and the left

and right side walls. The shape factor, F , for two parallel plates (back wall to stack) was known to be 1, and for two perpendicular plates (all else), it was known to be approximately 0.5.

4.3 Conductive Heat Transfer

Heat is also conducted along the stack, both through the ceramic stack material and through the air contained within the stack's pores. The fraction of the cross-sectional area of the stack which is occupied by the air is $GasA/A$. The solid cross-sectional area is $1 - (GasA/A)$. This partitioning leads to the definition of a stack "effective" thermal conductivity, k_{eff} .

$$k_{eff} = \frac{k_{solid}A_{solid} + k_{air}A_{gas}}{A_{solid} + A_{gas}} = k_{solid} \left(1 - \frac{GasA}{A} \right) + k_{air} \frac{GasA}{A}$$

For the 400 cells/in² Celcor used in this experiment, $GasA/A = 0.75$. Based on the manufacturer's values, $k_{solid} = 2.5 \pm 0.5$ W/m-°C, and the thermal conductivity of air was taken to be its room temperature value, $k_{air} = 0.026$ W/m-°C. Using these values, the thermal conduction through the air is less than 3% of k_{eff} , so its effects will be ignored, since the uncertainty in the manufacturer's value of the ceramic's thermal conductivity is $\pm 20\%$.

The conductive heat transfer rate within the Celcor stack was then calculated utilizing the conduction equation.⁴²

$$q_{cond} = k_{solid}A_{solid} \frac{\partial T}{\partial x} \cong k_{solid}A_{solid} \frac{\Delta T}{\Delta x}$$

The heat flow is in the x -direction and the temperature gradient dT/dx were assumed to be linear, where ΔT is the temperature change across the entire Celcor stack and Δx is the total length of the stack. This equation was programmed into an Excel spreadsheet, where the value k_{solid} was guessed and eventually calculated as will be described. The resulting value of k_{solid} was in agreement with the manufacturer's specifications (see Table 3).

4.4 Latent Heat

The heat which exits the ambient temperature end of the stack, *via* the finned heat exchanger, enters the water bath and melts ice. We determined that heat flow using the measured mass of ice melted vs. time.⁴²

$$q_{LH} = \lambda \frac{dm}{dt} \cong \lambda \frac{\Delta m}{\Delta t}$$

λ is the enthalpy of melting of the ice (333.55 J/g), m is the mass of the melted ice, and t is time. The melting rate of ice was approximated to be linear between each mass measurement. The average rate of melting was found for each block of ice by taking the change of mass from when the ice was put into the water bath until the ice was taken out. This change in mass was then divided by the amount of time that each ice block spent in the ambient duct water bath. Because temperatures on the hot side of the stack increased throughout the entire experiment (see Figure 20), the melting rate of the ice also increased. The melting rates of the ice were recorded at the times when the ice was removed from the water bath, then replaced with a “fresh” block. Assuming that initially there is no heat transfer going out of the duct (as the experiment was started when all of the parts of the resonator were at ambient temperatures), the melting rate was assumed to be zero at the start of the experiment. This produced a linear, time dependent function of melting rate. To show the amount of energy flowing out of the resonator (q_{LH}), the melting rates were multiplied by the latent heat constant. Figure 22 shows this result in a least-squares fit coefficient $R^2 = 0.9975$, corresponding to a statistical uncertainty of $\pm 5\%$.

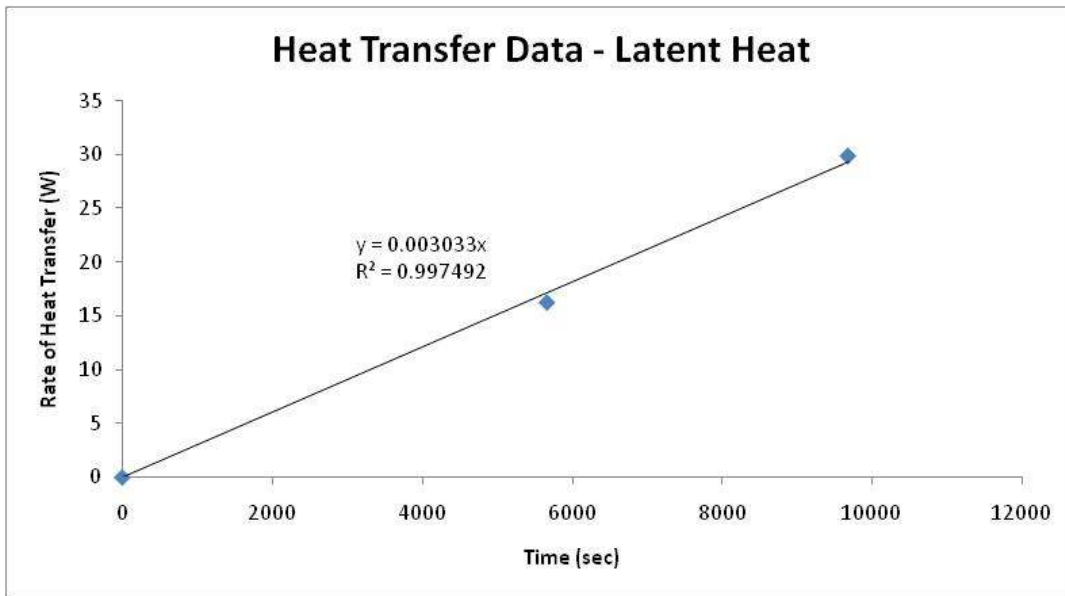


Figure 22: Rough correlation between the latent heat transfer data as a function of time. The increase in the heat flow rate is a result of the hot side temperature increase throughout the test. The equation for the linear trendline was used in the final heat transfer equations.

4.5 Results

There are three unknowns in the overall heat transfer budget: emissivity of the hot duct walls, absorptivity of the Celcor stack, and the conductivity of the stack. Values for these properties are initially guessed and then “solved” using the “Data Solver” add-in to minimize the squared deviation between the measured and modeled data.

First, q_{rad} was calculated using the equation discussed earlier and the guessed values of emissivity and absorptivity. This was then used to calculate a theoretical temperature difference in the Celcor stack.

Rearranging the equations, ΔT can be calculated using the value of q_{LH} determined from the ice melting data:

$$\Delta T = \frac{q_{rad} - q_{LH}}{kA} \Delta x$$

A theoretical hot stack temperature was found using the experimental values of the cold side stack temperature readings and the value of ΔT that was calculated above at each data point.

$$T_{hot} = T_{cold} + \Delta T$$

At each set of a data points, the difference between the theoretical and experimental temperatures were calculated within the spread sheet. These values were summed to produce a “total error”. Using Excel’s “Data Solver” add-in, the error was automatically minimized by simultaneously adjusting the unknowns. To check the validity of the solver’s results, the theoretical temperature was plotted against the experimental temperature of the Celcor stack hot-side. This demonstrated that the new values for the three major unknowns are a good approximation given the assumptions made as shown in Figure 23.

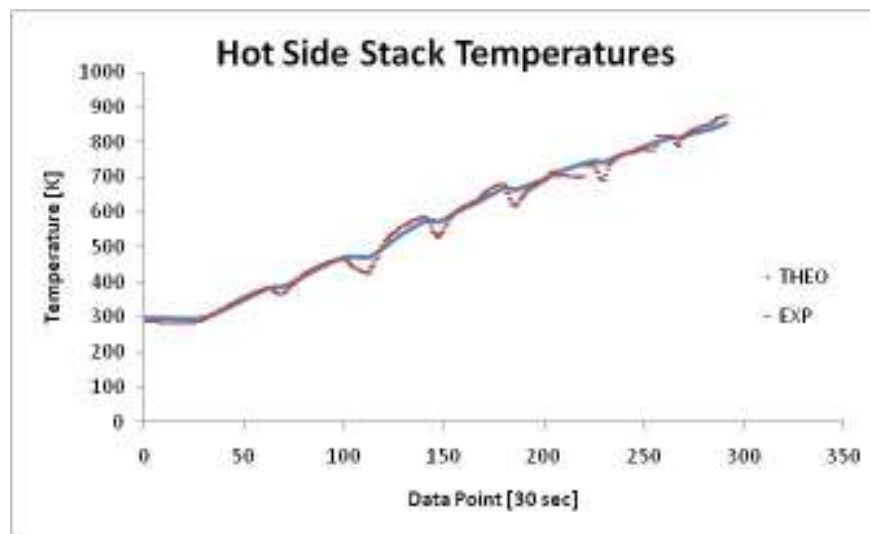


Figure 23: Theoretical and experimental hot-side temperatures for the Celcor stack. Experimental temperature values were taken as an average of the two hot-side E-type thermocouples. The theoretical temperature plot shown is a result that incorporates values determined by the Excel “Data Solver” add-in to calculate ϵ , α , and k_{solid} summarized in Table 1.

This method yielded the values for the unknowns shown in Table 3.

Symbol	Value	Units	Notes
ϵ	1	-	Value for "black-body" material (ideal emitter)
α	0.867375	-	Seems reasonable since the stack was "blackened" with soot before the start of the experiment. Ceramic is normally around 0.6 otherwise.
k	2.827954	W/(m-K)	Manufacturer's value was given as 2.5

Table 3: Parameter values determined by the Excel "solver" to minimize error between measured temperature and the radiative heat transfer equation.

Given these values, the total radiative heat transfer traveling from the walls of the hot duct to the hot end of the Celcor stack (q_{rad}) resulted in the following illustrated in Figure 24.

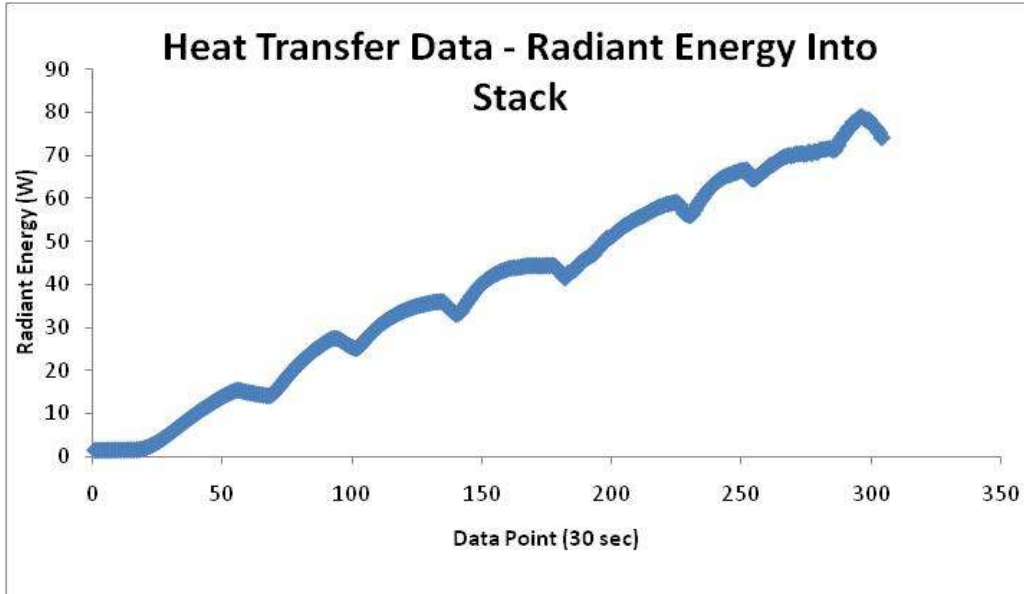


Figure 24: Rate of radiant heat transfer from the hot duct to the hot side of the Celcor stack. The heat transfer increases as the temperature of the duct was increased. The steps in the heat transfer vs. time are evident. As the electrical heater power is increased, the heat transfer to the stack increases then decreases slightly as the temperature of the hot-end of the stack increases resulting in more thermal energy being re-radiated from the stack back into the hot duct.

CHAPTER 5
HELMHOLTZ RESONATOR

Before testing was done with the linear alternator fastened to the resonator, testing was done with the apparatus set up as a Helmholtz Resonator. This resonator consisted of the normal resonator discussed throughout these reports, only in the Helmholtz mode; the linear alternator was replaced with a Polyvinyl Carbonate (PVC) pipe with the end open to the environment.

Four main variables were analyzed in the experimentation of the Helmholtz Resonator: the length of the Celcor stack, cell density of the stack, presence of the wedge in the ambient temperature duct, and the positioning of the heat exchanger.

The purpose of onset testing for the Helmholtz Resonator was to find a maximum efficiency and the corresponding dimensionless center position of the stack, kx . The wave number is equal to k , the wave number scaled by the acoustic wavelength $\lambda = 2\pi/k$ in the standing wave field, times x , a characteristic length equal to the distance from the center of the stack to the end of the hot duct. The importance of this value is due to the fact that both pressure magnitude and velocity are functions of kx :

$$p_1 = P \cos(kx) e^{j\omega t}, U_1 = U \sin(kx) e^{j\omega t}$$

At small values of kx , the pressure magnitude is high, but the velocity is very small. The opposite is true for larger values of kx . This information is vital when investigating the overall performance of the prototype (including linear alternator) since the product of pressure and velocity magnitudes are proportional to the energy extraction of the engine.⁶ By eventually testing the experimental setups with the linear alternator fastened instead of the resonator neck, an optimal kx can be found. In the future stages that will occur after the completion of this thesis project, kx will be used to scale the next prototype using similitude.

$$\Delta \dot{E} = \frac{A \Delta x}{4r_h} \left[\frac{(\gamma - 1) |p_1|^2 \delta_x \omega}{\gamma p_m} \left(\frac{\Gamma}{(1 + \sqrt{\sigma}) \Lambda} - 1 \right) - \frac{\rho_m |U_1|^2 \delta_v \omega}{A^2 \Lambda} \right],$$

where

$$\Gamma = (dT_m/dx)/\nabla T_{crit}$$

$$\nabla T_{crit} = \omega A |p_1| / \rho_m c_p |U_1|$$

$$\Lambda = 1 - \frac{\delta_v}{r_h} + \delta_v^2 / 2r_h^2$$

Where ΔE is the amount of extractable energy, r_h is the hydraulic radius of the stack cells, γ is the specific heat ratio of the gas, δ_x is the thermal penetration depth, p_m is the mean static pressure, σ is the Prandtl number of the gas, ρ_m is the mean density of the gas, δ_v is the viscous penetration depth, T_m is the mean temperature of the gas, and c_p is the specific heat capacity at constant pressure of the gas.

The dimensionless stack position was manipulated three ways. By removing the ambient temperature duct wedge, the resulting frequency would change due to the change in the compliance of the air in the duct. The heat exchanger, also in the ambient temperature duct, was moved 2 cm closer to the hot end of the resonator. This forces the stack to sit 2 cm closer to the end due to the fact that the cool side of the stack sits directly adjacent to the heat exchanger. Three different lengths of stack were used: 10 cm, 7.5 cm, and 5 cm. Finally, different lengths of resonator necks were used to change the amount of oscillating air within the resonator for each test scenario. This in turn, changes the frequency; the longer the neck, the lower the frequency. As all three of these parameters were changed, the resulting pressure magnitudes were recorded with their corresponding resonator neck lengths.

Three Celcor cell densities were tested; a 400 cell/in² Corning Celcor ceramic,⁴³ and 100 and 200 cell/ in² Celcor stack produced by Jiangxi Tianmei New Environmental Material Co.⁴⁴ The different types of Celcor have different surface area to volume of air ratios. This changes the properties of the conduction from air-to-stack and stack-to-air, as well as changes the amount of air that is affected by viscous drag due to the walls. Therefore, it is vital to find a balance between heat transfer and viscosity of the moving air within the stack. The different frequencies, stack lengths, and heat exchanger positions will also result in changes to the heat transfer properties of the resonator.

Prior to the resonator reaching onset, the free-decay of the standing wave was recorded at various temperature gradients across the Celcor stack. The decaying sound wave is simply the result of exciting the air within the resonator manually by rapidly uncapping the Helmholtz neck. The properties of the decaying wave were used to calculate the overall system Quality Factor of the resonator at different values of temperature difference ΔT across the stack. This was done to determine the pre-onset characteristics of the resonator, especially when comparing two different sets of data.

5.1 PreOnset Measurements

Since there is no loudspeaker within the Helmholtz Resonator, the air was excited impulsively by removing a PVC cap from the PVC neck protruding from the resonator. The resulting decaying wave was recorded by the Endevco Model 8510B-2 (S/N: APJ50) piezo-resistive differential pressure sensor as the internal microphone located within one of the instrument doors on the side of the ambient temperature duct and connected to a Digital Signal Oscilloscope (DSO) set in the "Triggered" mode. The trigger was set to a known voltage amplitude, which was reached when the PVC cap was quickly removed. The piezo-resistive sensor is configured as a resistive Wheatstone bridge. The differential bridge output voltage was also applied directly to the differential inputs of a Stanford Research SR-560 Low-Noise Voltage Preamplifier. The inputs to the preamplifier were ac-coupled. The amplifier provided an adjustable gain (set to x10 for these experiments) and also included a user-selectable low-pass and high-pass filter. The filters were set to 3 Hz and 3 kHz to exclude any extraneous out-of-band noise. The SR-560 provided access to its $\pm 12 V_{dc}$ power supply that was used to provide power to the head amp that provided the $\pm 5.00 V_{DC}$ bridge bias voltage. A typical free-decay wave signal can be seen in Figure 25.

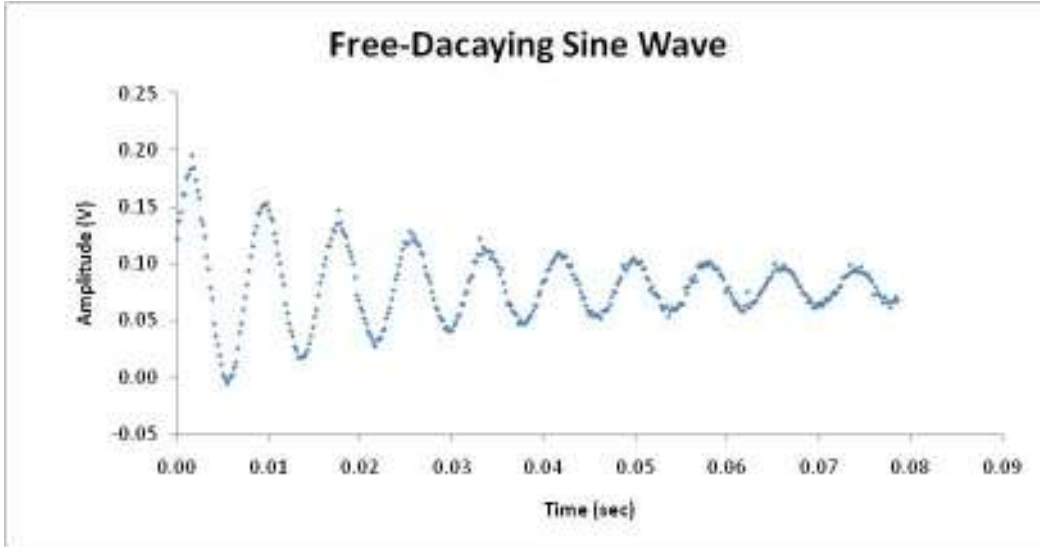


Figure 25: Typical free-decay wave signal produced by the impulsive excitation of the resonator by removing a cap from the Helmholtz neck. This plot was acquired by the HP 54621A Digital Signal Oscilloscope and recorded on a floppy disk drive. The file is loaded on to a computer from the floppy disk and is opened and plotted in Excel. This test was done using a 2.06 inch Helmholtz neck length and a stack at ambient temperature ($\Delta T_{stack} = 0 \text{ }^\circ\text{C}$).

This decaying signal should obey the following equation that has five parameters that can be adjusted to fit the equation to the measured data:

$$v(t) = Ae^{t/\tau} \sin(2\pi ft + \Phi) + V_{DC}$$

A is the initial magnitude of the signal, τ is the decay time, f is the resonance frequency, Φ is the phase offset, and V_{DC} allows for the possibility that the measured signal includes a DC offset. Using Excel’s “Data Solver” add-in, the unknown parameters, A , τ , f , Φ , and V_{DC} , were varied to minimize the square error summation between the experimental data and the theoretical values generated by the model equation. This process was much like the process explained in the “Heat Transfer Spreadsheet” portion of this report. The theoretical and experimental time-dependent voltages are plotted on the same graph in Figure 26. As one can see, the data extracted from the linear alternator matches extremely well with the theoretical data calculated from the equation above when the error is minimized.

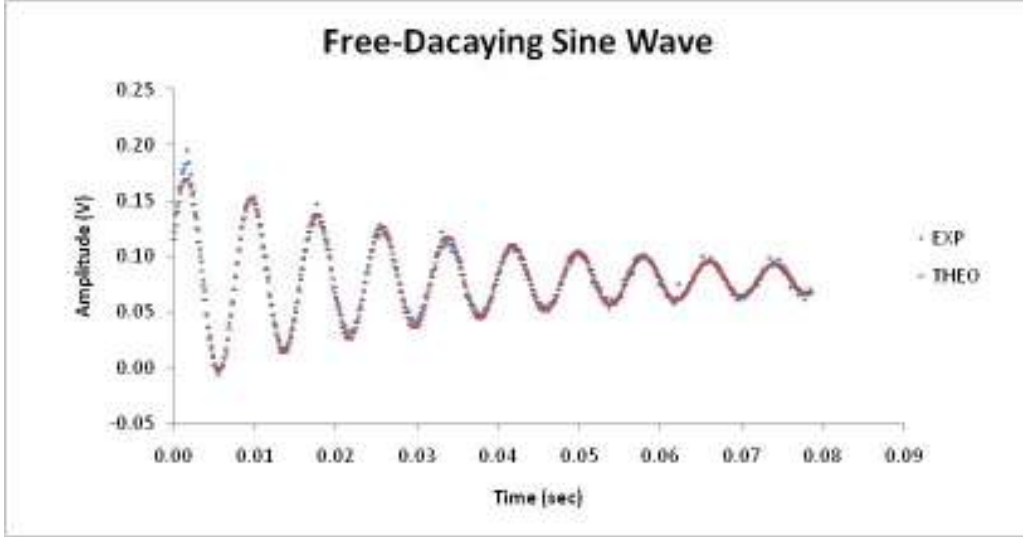


Figure 26: Measured voltages (•) are compared to the theoretical decay waveform voltages (•) after the Excel “Data Solver” function adjusted the five waveform parameters (A , τ , f , Φ , and V_{DC}) to minimize the square difference between the measured and calculated voltages. This test was done with a Helmholtz neck length of 2.06 inches and the stack at ambient temperatures ($\Delta T_{stack} = 0\text{ }^{\circ}\text{C}$).

The Quality Factor, Q , was then found using the equation below relating Q to frequency f and exponential decay time τ :

$$Q = \pi f \tau$$

As the average temperature gradient across the stack becomes larger, the Q should approach infinity. Q is infinite when the resonator is at onset. To avoid an infinite result, the reciprocal of $Q = 1/Q$ is plotted against the temperature difference as shown in Figure 27.

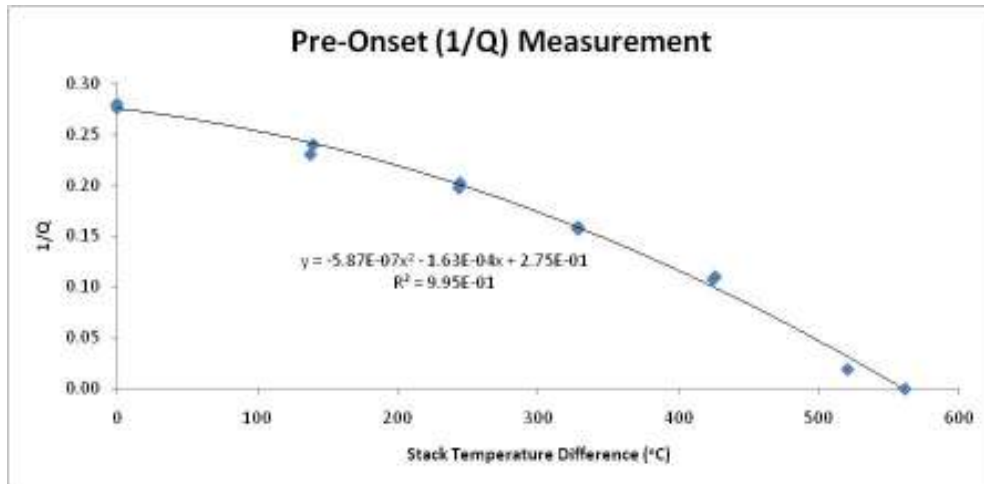


Figure 27: Test was done with a Dayton DA115-8 4” driver. The stack used was a 10 cm long, 400 cell per square inch Celcor ceramic stack. Pre-onset $1/Q$ recordings at various stack temperature differences. Q increases towards infinity as the temperature gradient nears its critical value. The stack had a temperature difference at onset of $\Delta T_{crit} = 561.1\text{ }^{\circ}\text{C}$. The extrapolation to $Q = \infty$ occurs at $\Delta T_{crit} = 559.6\text{ }^{\circ}\text{C}$.

To link the temperatures across the stack to the free-decay time, free-decay measurements were done while the LabVIEW program was running. This was the same LabVIEW code used in the Heat Transfer portion of this thesis (Chapter 4) and as seen in Figures 17 and 18. The time at which the decay data were recorded by the DSO was noted and the corresponding temperature data was extracted from the Excel file produced by LabVIEW.

The best example of using free-decay measurements for the use of characterizing the resonator is to investigate the viscous losses within the Celcor stack. The affects of viscous losses in the resonator are dominated by the Celcor stack. This makes sense theoretically since the surface area within the stack is much greater compared to the walls of the resonator and resonator neck. This is can be quantified by investigating the Quality Factor at ambient temperatures and varying the parameters of the Celcor stack (length, cell density). This relationship can be seen in Table 4.

Q At Ambient Temperatures				
		Stack Length [cm]		
		10	7.5	5
Cell Density [cps]	400	7.78	-	12.52
	200	12.52	12.73	13.99
	100	-	14.82	15.45

Table 4: The Quality Factor of the Helmholtz Resonator was investigated to show the effects of viscous losses within the apparatus. The higher cell density and longer stack increases the “wetted” surface area; the surface area in contact with the oscillating air.

5.2 Onset Measurements

Initial calculations were performed in Excel to attain an estimate of the required neck diameter $(4s/\pi)^{1/2}$ and length L before the initial experiments were performed on the Helmholtz Resonator.

$$f = \frac{c}{2\pi} \sqrt{\frac{s}{VL_{eff}}}$$

f is the resonance frequency, c is the speed on sound in air, s is the area of the neck, V is the volume of the resonator, excluding the neck, and L_{eff} is the effective length of the neck which is calculated from the measured length L of pipe to accommodate the kinetic energy of the moving gas directly in front of the neck.

$$L_{eff} = L + 1.7r$$

The lengths of neck ranged from one to 17 inches to guarantee a pressure “cross-over” to find a moving mass that corresponded to a maximum pressure magnitude. The pressure crossover and resulting frequency is shown in Figure 28. The measurements taken from the HP 34970A Data Acquisition Unit and relayed to LabVIEW were of the Endevco piezo-resistive microphone AC Voltage and frequency, as well as the standard temperature data to calculate the temperature change across the stack. By performing a simple microphone calibration test (see Appendix B), the resulting pressure amplitude can be attained from the voltage output corrected for the gain of the SR-560.

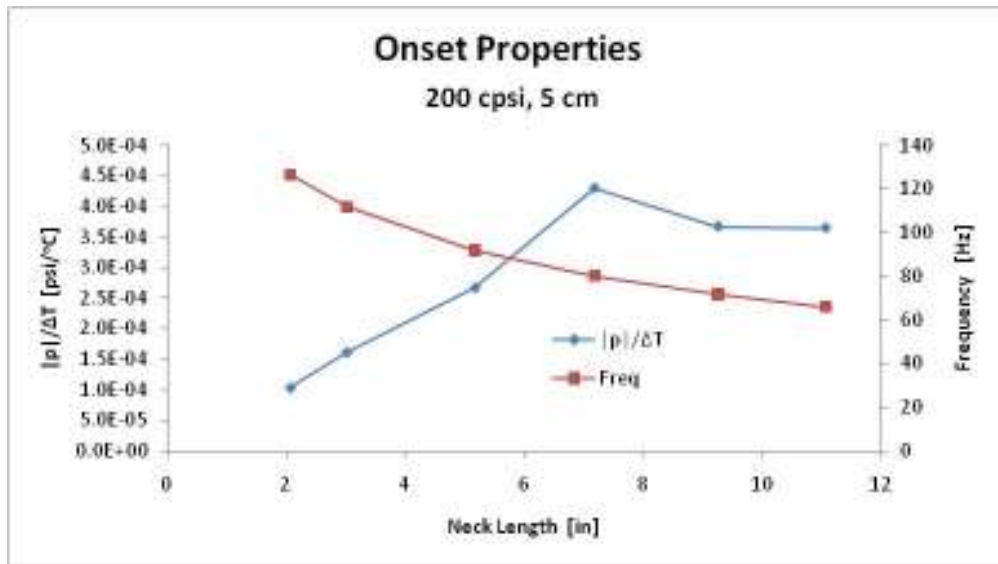


Figure 28: Pressure (•) and frequency (•) measurements for various resonator neck lengths. All measurements were made with a stack temperature difference of approximately 300 °C. A 200 cell/in², 5 cm long Celcor stack was used. The pressure magnitude per difference in stack temperature was used to accommodate for any slight variations of temperature during testing. The resonator neck resulting in the highest pressure magnitude was used for future measurements.

Experiments were done, varying many parameters: the Celcor stack length, stack matrix density, heat exchanger location, and presence of the wedge within the ambient temperature duct.

The effect of the Celcor stack length Δx , changes the dimensionless stack position kx . Experiments done with 5, 7.5, and 10 cm Celcor stack lengths, Δx , yielded the same trends regardless of the cell density of the stack. It has been observed that the shorter stack results in a larger acoustic pressure magnitude over similar temperature differences across the stack. Because the amount the smaller temperature difference required less heater energy, it was found that the shorter stack was optimal. This is shown in Figure 28 using 200 cell/in² Celcor, though this trend was consistent for all cell densities.

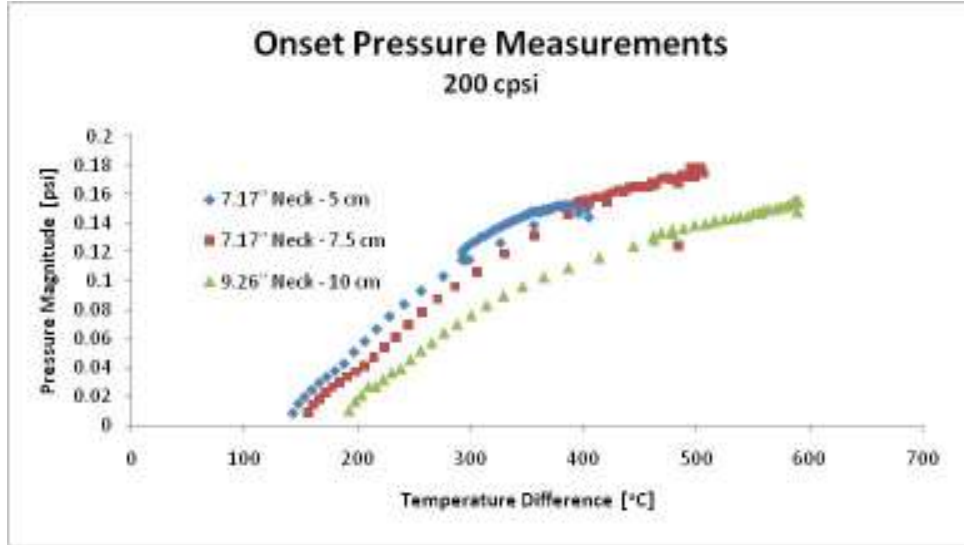


Figure 29: Pressure magnitude versus temperature difference across three different lengths of Celcor. All tests were done under similar conditions. A 200 cell/in² Celcor material was used, the ambient temperature duct wedge was removed, and the heat exchanger was moved 2 cm closer to the hot end of the resonator. The resonator neck length that produced the largest pressure magnitude was used for all three cases.

Since the optimal length of stack was found to be 5 cm long, testing was then focused to find the best Celcor cell density for this stack length. 400, 200, and 100 cell/in² Celcor was used under similar experimental set up. This trend is shown in Figure 30 for a stack length of about 5 cm in each of the three cases. As discussed earlier, there is a balance between viscous losses and heat transfer in the Celcor stack for changing cell densities. To characterize this, a dimensionless number equal to the hydraulic radius of an individual cell over the thermal penetration depth is equated and investigated. This number is commonly known as the Lautrec number, La .⁴⁵ Table 5 shows the Lautrec number as well as the thermodynamic properties of the air at the hot end and the cold end of the 5 cm Celcor stack used in the data for Figure 30. From the data acquired, the 100 cell/in² Celcor stack material resulted in the highest pressure magnitude for the best-case-scenario resonator neck length.

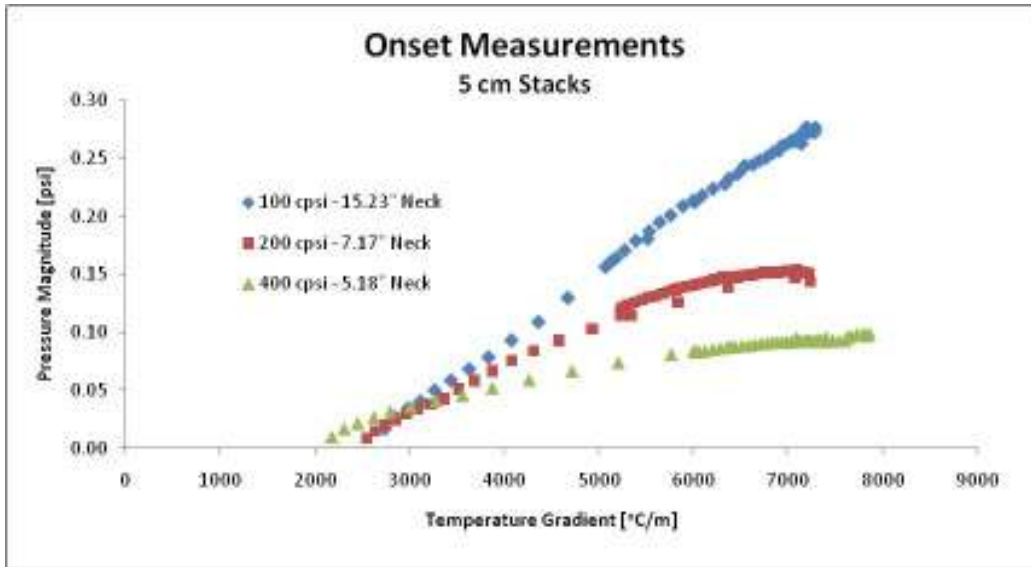


Figure 30: Pressure magnitude as a function of temperature gradient across three Celcor stack densities. All three tests were done under similar circumstances. The stack was approximately 5 cm long, the heat exchanger was positioned 2 cm closer to the hot end of the resonator, and the wedge was taken out of the ambient side duct. For each case, the length of resonator neck that produces the highest pressure magnitude was used. The 400, 200, and 100 cpsi stacks (•, •, •) had a 15.23, 7.17 and 3.01 inch neck, resulting in a 58, 80, 94 Hz frequencies, respectively.

		100 cell/in ²		200 cell/in ²		400 cell/in ²		
		HOT	COLD	HOT	COLD	HOT	COLD	
α	m ² /sec	8.09E-05	2.88E-05	8.87E-05	3.18E-05	7.97E-05	2.90E-05	m ² /sec
ω	rad/sec	344.9		505.2		588.1		rad/sec
δ_k	m	6.85E-04	4.09E-04	5.93E-04	3.55E-04	5.21E-04	3.14E-04	m
r_h	m	2.70E-04		1.92E-04		1.36E-04		m
La	-	0.39	0.66	0.32	0.54	0.26	0.43	-
La_{avg}	-	0.53		0.43		0.35		-

Table 5: Lautrec number for cold and hot sides of the Celcor stack for tests shown in Figure 30. As cell density decreases, the Lautrec number increases.

Finally, the effects of volume exclusion were investigated. The presence of the ambient duct wedge was used to see how the pressure would change. By removing volume in the duct, the stiffness of the air will increase and the amount of energy lost to the compliance increases. Because the ambient side of the duct was open to the environment *via* the resonator neck, it was predicted that removing the wedge would result in only a slight increase in pressure magnitude. However, this plays a much bigger role when the resonator was connected to the linear alternator (as seen in Section 6.2). This prediction was further analyzed when investigating a DELTAEC program of the resonator in Helmholtz mode. The results of these two DELTAEC codes can be seen in Figure 31. The DELTAEC code used for this plot can be seen in Appendix E.

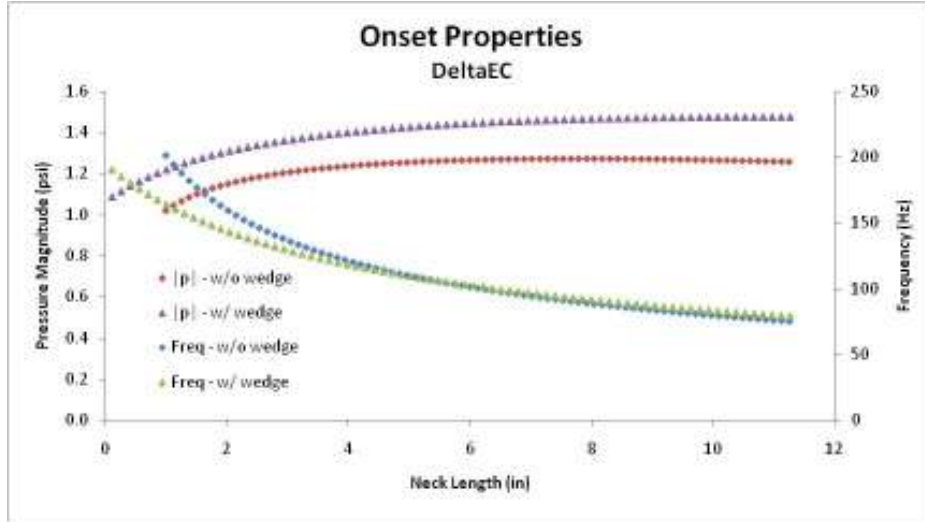


Figure 31: DELTAEC plot of varying neck length and the resulting Onset Properties, frequency (right axis), and pressure magnitude (left axis). Two similar codes were written, only differing in ambient temperature duct volume due to the presence of the wedge. The codes were written for a 5 cm long, 400 cell/in² Celcor stack. The temperature difference across the stack was 300 °C. The heat exchanger was positioned closer to the hot end of the resonator. All the geometries matched that of the Helmholtz Resonator as built.

Comparing two sets of data taken from experiments that only varied in ambient temperature duct volume, the effects in the change of compliance can be seen in Figure 32. As predicted theoretically and in DELTAEC, this only resulted in a relatively small change in performance.

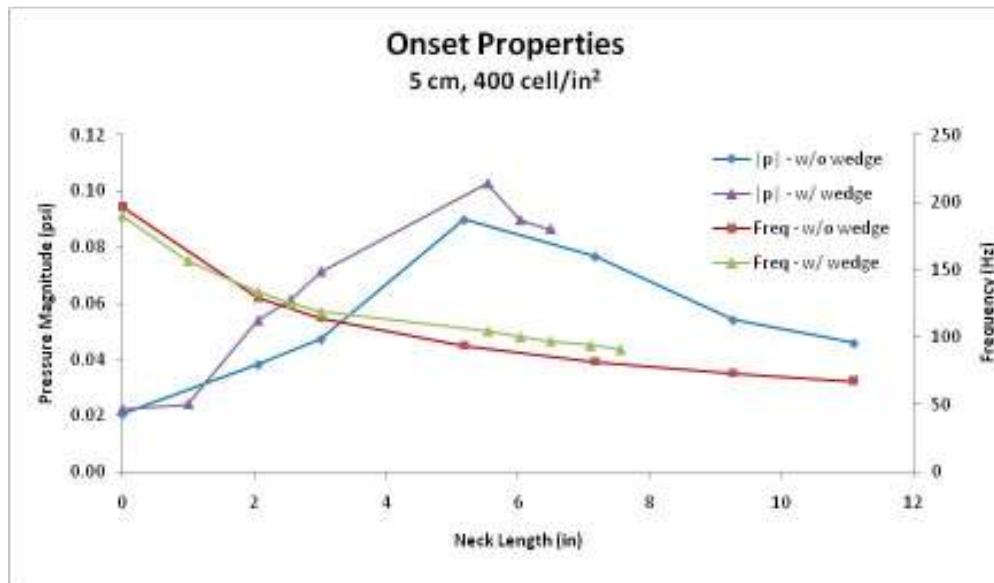


Figure 32: Onset properties varying ambient temperature duct volume. Test was done using a 5 cm, 400 cell/in² Celcor stack. The difference in stack temperature was approximately 300 °C for all measurements. The heat exchanger was positioned closer to the heat end of the resonator. The resonator with the wedge present produced a slightly greater pressure magnitude, as predicted theoretically and by DELTAEC.

The summary of all Helmholtz Resonator Tests can be seen in Table 6. These results were used for testing with the apparatus in power production mode.

Test		1	2	3	4	5	6	7	8	9	10	
Date		8/18/2010	8/19/2010	8/25/2010	8/28/2010	9/1/2010	9/7/2010	9/8/2010	9/10/2010	9/14/2010	9/15/2010	
HX Pos		Far	Far	Close	Close	Close	Close	Close	Close	Close	Close	
Wedge		Yes	Yes	Yes	Yes	No	No	No	No	No	No	
Stack	cm	5	10	5	10	5	10	7.5	5	7.5	5	cm
Cell Density	cpsi	400	400	400	400	400	200	200	200	100	100	cpsi
x	m	0.1435	0.1670	0.1470	0.1235	0.1470	0.1235	0.1353	0.1470	0.1353	0.1470	m
Q (AMB)	-	9.19	7.78	11.11	8.23	12.51	12.52	12.731	13.99	14.82	15.45	-
ΔT_{stack}	$^{\circ}C$	157.50	264.43	155.20	261.77	154.37	300.959	195.862	193.55	315.248	254.08	$^{\circ}C$
$(p /\Delta T)_{max}$	psi/ $^{\circ}C$	2.62E-04	2.38E-04	2.74E-04	2.61E-04	3.05E-04	2.56E-04	4.05E-05	4.30E-04	5.47E-04	6.48E-04	psi/ $^{\circ}C$
L_{max}	in	3.01	3.01	3.01	9.26	5.18	9.26	7.17	7.17	13.65	15.24	in
f_{max}	Hz	118.29	121.18	118.49	79.03	93.61	72.54	81.33	80.04	59.22	54.88	Hz
c	m/s	434.49	460.4	437.14	469.41	452.79	469.56	466.25	439.87	465.85	440.58	m/s
$(kx)_{max}$	-	0.245	0.276	0.250	0.131	0.191	0.120	0.148	0.168	0.108	0.115	-

Table 6: An overview of all Helmholtz mode resonator tests. This table was used to determine the best experimental setup and the resulting dimensionless wave number. Because power extraction is a function of pressure *and* velocity magnitude, three setups (3, 8, 10) were used for future engine experimentation.

There are some parameters that can be observed to be optimal, even before testing was done while the resonator was in power extraction mode. Firstly, it is obvious that the shortest stack, 5 cm, was better than the other two lengths of stack. This shorter stack limited the amount of viscous losses as well as balanced the conductive heat transfer through the resonator while keeping the temperature difference at a level where onset occurred. This was true for all cell densities. Secondly, the 100 and 200 cell/in² Celcor stacks clearly outperformed the 400 cell/in² stack. Again, the larger cell sizes limited the viscous losses in the resonator, but also allowed for the air “blobs” to move at a larger percent of the free stream velocity. In other words, the small cells restricted flow through the stack, ultimately choking the movement of the oscillating air. For the next set of tests, only these parameters were investigated and at the corresponding dimensionless wave number for each test was kept consistent by varying the frequency. This process is explained to greater detail in the next chapter.

CHAPTER 6 THERMOACOUSTIC ENGINE

The ultimate goal of this thermoacoustic project is to convert a small amount of the heat produced by biomass combustion in a cook stove to electrical power. To test this process quickly, and at minimal expense, we used commercially-available, inexpensive four inch (nominal) diameter electrodynamic loudspeakers as the linear alternator sealed to the resonator. As discussed in the prior section, the parameters investigated in these series of experiments involve stack position and density, volume exclusion, and driver type. Operating frequency was varied by the addition/subtraction of mass from the driver cone for all tests. This was done to find the dimensionless stack position number corresponding to the highest level of power extraction for each case.

6.1 PreOnset Data

A sine wave signal was generated by a HP3314A Function Generator and sent to an HP467A Power Amplifier. This amplified signal then ran through the simple trigger synchronization mechanism shown in Figure 33. This trigger mechanism was connected directly to the linear alternator sealed to the resonator. This switch box was used to simultaneously disconnect the driving signal generated by the function generator and send the resulting “decaying” electronic signal produced by the subsequent motion of the loudspeaker’s voice coil motion in the magnet gap to an HP54621A Digital Signal Oscilloscope. This DSO was set in “Trigger Mode” which would initiate a single trace if the signal went below a certain threshold. The DSO displays the decaying sine wave generated by the linear alternator’s motion. The resulting sweep was then saved to a floppy disk and transported to a computer where the file was read and plotted in Excel. From here, the same procedure used in the Helmholtz mode pre-onset (see Section 5.1) was performed to calculate the decaying wave properties. A trace obtained this way is shown in Figure 34.

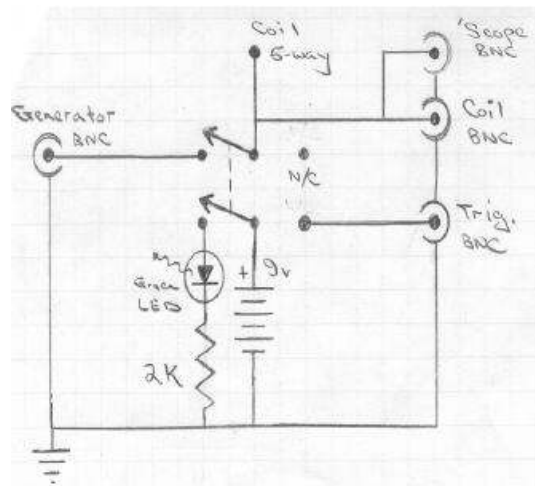


Figure 33: Circuit schematic of the switch-box trigger system. One pole of the double-pole, double throw toggle switch connects the generator to the voice coil and to the oscilloscope while lighting a green LED. When the switch is thrown in the other direction, the coil is still connected to the oscilloscope and the generator is disconnected. The 9V battery provides the signal that triggers the ‘scope trace.

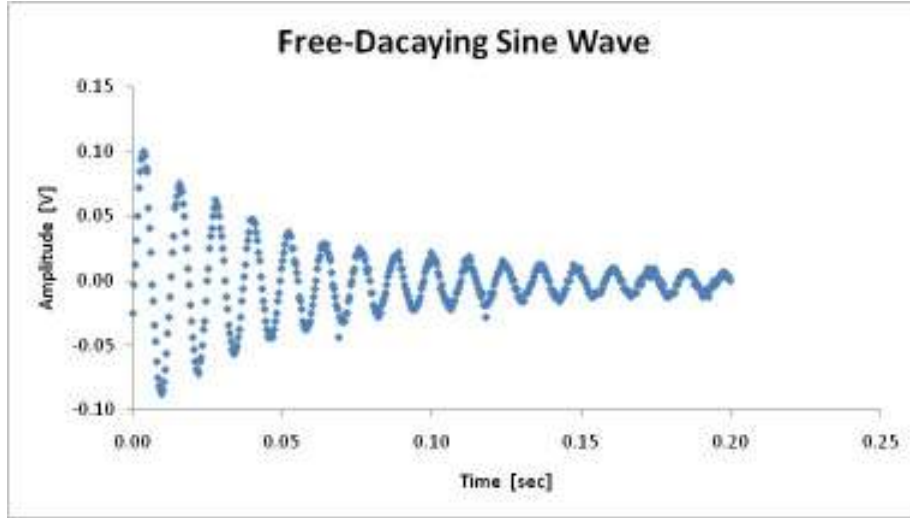


Figure 34: Example of a free-decay measurement using the trigger mechanism as seen in Figure 30. The loudspeaker used in this example is the Dayton 4" (nominal) ND105-4. The resonator was at ambient temperature, so there was no temperature difference across the 5 cm, 100 cell/in² Celcor stack.

The mechanical power Π_{mech} dissipated by the speaker's motion is related to the speaker's mechanical resistance R_m :

$$\Pi_{mech} = \frac{1}{2} R_m v_1^2$$

Faraday's Law provides the peak velocity of the voice coil v_1 in terms of the r.m.s. voltage V_{ac} developed across the voice coil and load resistor:

$$v_1 = \frac{\sqrt{2} V_{ac}}{B\ell}$$

Free decay measurements of the speaker's mechanical resistance when mounted in the resonator, and when tested in free-space, indicated that the resonator losses were dominated by the speaker's losses. For the Dayton 115-8, the speaker's $R_m = 0.89$ kg/sec on the bench ($f_o = 62.44$ Hz) and $R_m = 1.09$ kg/sec when mounted on the resonator ($f_o = 119$ Hz), indicating that the equivalent mechanical resistance created by thermoviscous dissipation and other losses in the resonator was $R_{res} = 0.20$ kg/sec. This result suggests that the mechanical dissipation in the Dayton 115-8, exclusive of the effects of an external load resistor, accounted for nearly 82% of the mechanical losses in the complete resonant system at room temperature.

This high ratio of dissipation in the speaker, to losses in the resonator, indicates that high-efficiency electroacoustic power generation will require an electrodynamic alternator which has less intrinsic mechanical resistance. Although ultimately, a moving magnet linear alternator similar to the Bose LM-0 or a small version of the Q-Drive Model 1M102M/A will have lower mechanical dissipation and higher efficiency in a thermoacoustic application, we procured four Dayton ND105-4 speakers. As shown in Table 1, the Dayton ND-105 has lower R_m and a higher $B\ell$ -product that should improve overall electroacoustic conversion efficiency when it is installed after the optimum stack geometry (*i.e.*, kx , Δx ,

and r_h) is determined from the “Helmholtz Substitute Neck” experiments that were described in the previous chapter.

6.2 Onset Measurements

To measure power output of the loudspeaker, a variable resistor was shunted across the voice coil terminals. Once the resonator was at onset and the temperature difference across the stack was stable at approximately 400 °C, Voltage readings were taken across the linear alternator at various values of series resistance. All tests were done with 5 cm long Celcor stacks, so only temperature difference and not temperature gradient was used in the discussion of the onset experimentation. For each test, the optimal values of kx that were found in the Helmholtz mode tests were utilized. This was done by adding mass to the cone of the speaker using a sticky duct sealant until the resonance occurred at the frequency corresponding to the value of kx that was needed. During testing, the addition and reduction of mass was done allowing for power extraction measurements to be made for the immediate range of kx . An example of a full power extraction test is shown in Figure 35. For this example, the optimal frequency was about 54 Hz for Helmholtz mode testing and about 51 Hz for the resonator in power extraction mode.

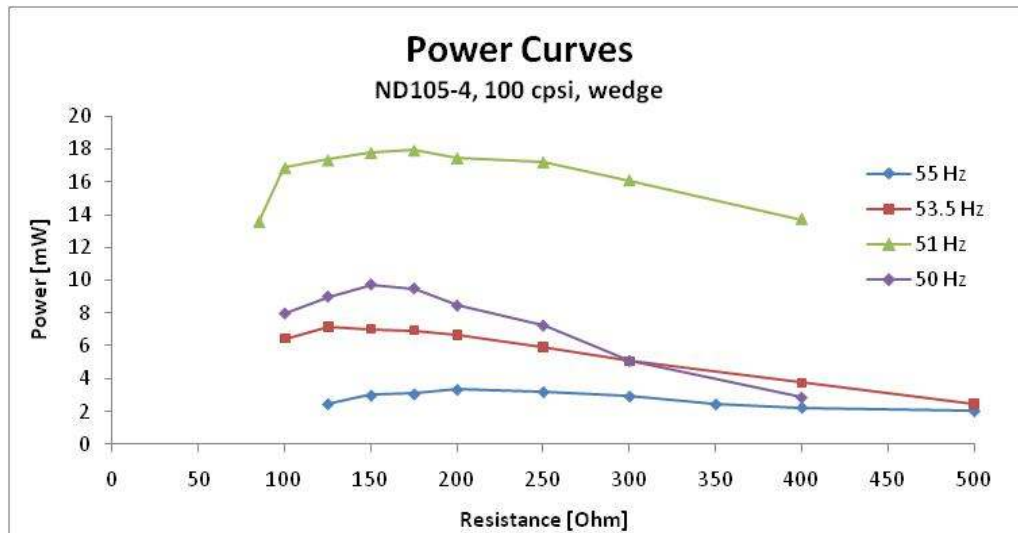


Figure 35: Power extraction measurements using the ND105-4. Testing was done using a 5 cm long, 100 cell/in² Celcor stack. The temperature difference across this stack was approximately 400 °C for all power measurements. The frequencies 55 (•), 53.5 (•), 51 (•), and 50 (•) Hz are the results of adding 32.0, 35.0, 38.0, and 41.2 grams, respectively.

The power “turn-over” (*i.e.* the area of decreasing power as electrical resistance is lowered) was investigated in Table 6 by examining the mechanical and electrical power dissipation ($\Pi_{elec} = IV$). This set of data was taken using the DA115-8 driver and the ambient temperature duct wedge.

Load Resistor (Ω)	Voice Coil (V_{ac})	Power (mW)	Velocity (m/sec)	Π_{mech} (mW)	Π_{elect} (mW)	Π_{elect}/Π_{mech} (%)
∞	1.603	0	0.45	99.8	0.00	0.00%
1000	1.544	2.38	0.44	92.6	2.38	2.57%
900	1.55	2.67	0.44	93.3	2.67	2.86%
800	1.55	3.00	0.44	93.3	3.00	3.22%
700	1.54	3.39	0.43	92.1	3.39	3.68%
600	1.53	3.90	0.43	90.9	3.90	4.29%
500	1.52	4.62	0.43	89.7	4.62	5.15%
400	1.46	5.33	0.41	82.8	5.33	6.44%
300	1.38	6.35	0.39	74.0	6.35	8.58%
200	1.24	7.69	0.35	59.7	7.69	12.87%
100	0.92	8.46	0.26	32.9	8.46	25.74%
∞	1.8	0	0.51	125.9	0.00	0.00%

Table 7: Mechanical power dissipation Π_{mech} in the Dayton 115-8 speaker and electrical power dissipation Π_{elect} in the load resistor. The overall dissipation created by for resistors below 100 Ω was sufficient to quench the thermoacoustic oscillations.

Initial measurements were done to investigate the power extraction of the two cell densities that resulted in the highest pressure magnitudes in the Helmholtz mode tests; 100 and 200 cell/in². Both stack lengths were approximately 5 cm long. The other resonator parameters were kept consistent, and the ND105-4 (#3) driver was used. Figure 36 shows the power extraction for the best values of kx for each case. The 100 cell/in² Celcor stack resulted in more power extracted for all values of resistance. The remaining Onset tests were therefore done using the 100 cell/in² stack.

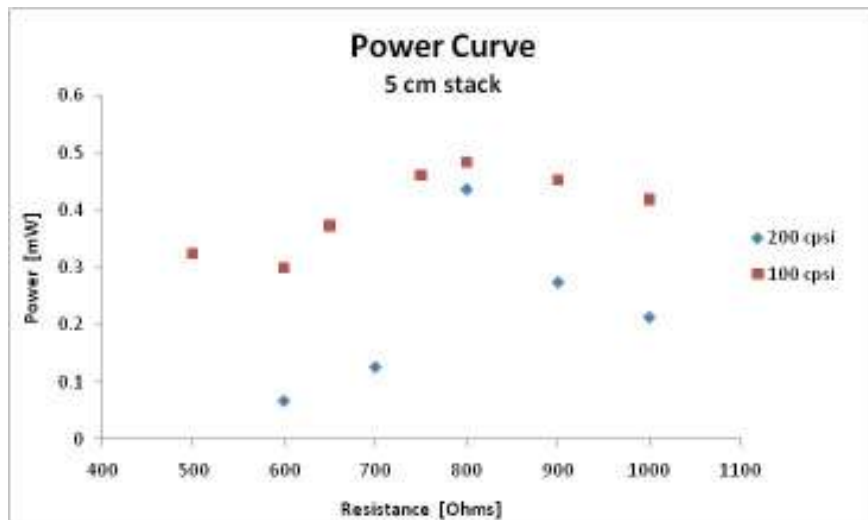


Figure 36: Power curve for two different cell densities. The curves shown were done at their respective maximum power values of frequency (of kx). The resonator had no wedge. The same ND105-3 driver was used for each test. The stacks measured approximately 5 cm long and the temperature difference across the stacks were each 400 °C.

The next sets of measurements were done to investigate the effects of volume exclusion. It was observed that when the resonator was in the Helmholtz mode, the reduction of ambient-side volume increased the performance (pressure magnitude). Because the resonator was now coupled with the linear alternator and not the resonator neck which was open to the environment, it was predicted that the reduction of ambient-side volume would drastically increase the power extraction. This would be due to the reduction of compliance within the resonator. When the pressure increases in this duct, instead of compressing the air that was displaced, the pressure would go into moving the linear alternator, thus increasing the power extraction. This was observed with each driver, the ND105-4 and the DA115-8. The results are shown in Figures 37 and 38. Volume exclusion for the DA115 tests (Fig. 37) was done using the wedge and the addition of the Balsa plunger to the cone. Tests done using the ND105 (Fig. 38) was only done using the wedge. It is clear that ambient temperature side duct volume plays a vital role in the engines overall performance. The total volume of the ambient temperature duct is 562.0 cm^3 , where the wedge and the plunger device are 183.5 cm^3 and 68.8 cm^3 , respectively. This means that the combination of the plunger and wedge in the duct results in a significant drop in volume, 45.1%.

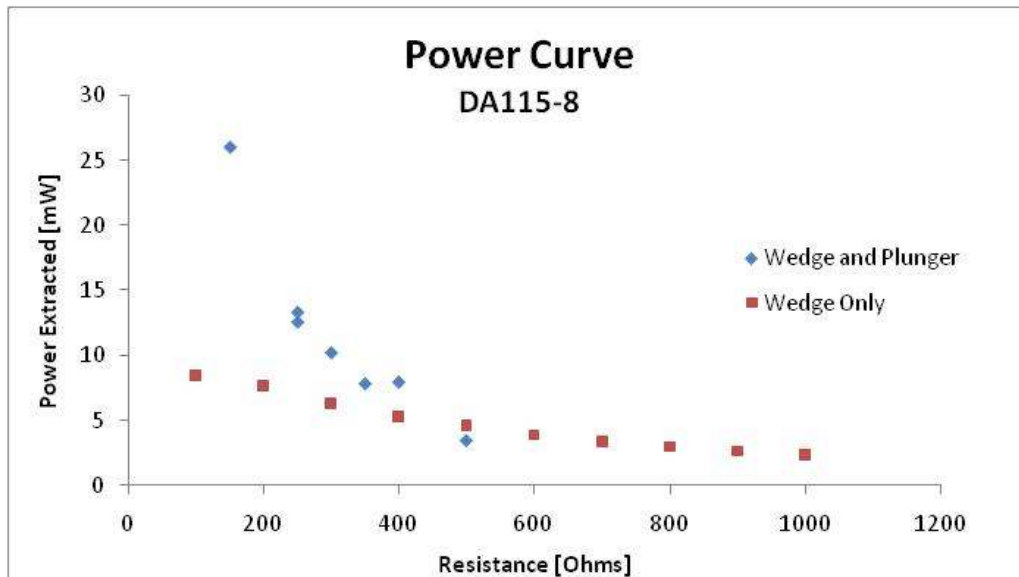


Figure 37: Power extraction measurements using the Dayton DA115-8 driver. Both tests were done under similar conditions. A 5 cm, 100 cell/in² Celcor stack was used. All measurements were taken with a stack difference in temperature of approximately 400 °C. One test (•) was done with only the wedge extracted volume from the ambient-side duct. The other test (♦) was done using both wedge and a Balsa wood plunger attached to the cone of the driver.

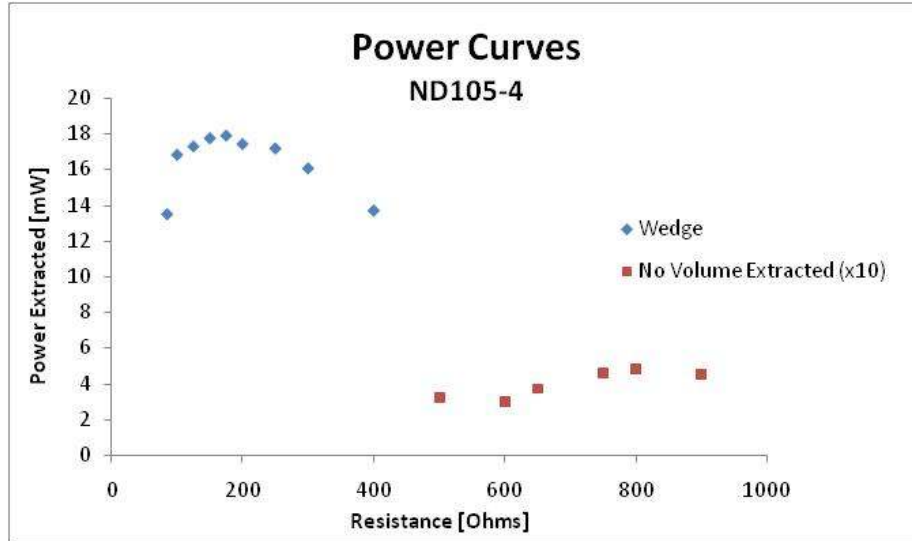


Figure 38: Power extraction curves using the ND105-4 driver. Both tests were done under similar conditions. A 5 cm, 100 cell/in² Celcor stack was used. All measurements were taken with a stack difference in temperature of approximately 400 °C. One test (•) was done with no volume extraction done in the ambient-side duct and was plotted ten times the measured value for convenience. The other test (•) was done using both wedge and a Balsa wood plunger attached to the cone of the driver.

The two experimental setups that resulted in the most power extracted had the 5 cm long, 100 cell/in² Celcor stack, and the ambient temperature duct wedge. One setup had the Dayton DA115-8 driver with the Balsa wood plunger attached, and the other used the ND105-4 loudspeaker. Both tests resulted in approximately 18-24 mW of maximum power extracted at a stack temperature difference of about 400 °C. A summary of all of the tests done can be seen below in Table 8.

Test		1	2	3	4	5	
Date		9/21/2010	9/24/2010	10/1/2010	6/23/2010	9/29/2010	
Driver		ND105-4	ND105-4	ND105-4	DA115-8	DA115-8	
Wedge	-	No	No	Yes	Yes	Yes	-
Plunger	-	No	No	No	No	Yes	-
Stack	cm	5	5	5	5	5	cm
Cell Density	cpsi	100	200	100	100	100	cpsi
x	m	0.1470	0.1470	0.1470	0.1470	0.1470	m
Q (AMB)	-	11.51	17.98	9.53	3.59	8.91	-
ΔT _{stack}	°C	400.43	391.79	392.56	391.10	397.23	°C
P	mW	0.46	0.44	17.91	8.46	25.98	mW
f _{max}	Hz	50.27	55.07	51.22	53.45	53.12	Hz
c	m/s	479.72	475.03	469.07	469.68	464.50	m/s
(kx) _{max}	-	0.097	0.107	0.101	0.105	0.106	-

Table 8: Overall data taken from power extraction tests.

DELTAEC was used throughout power extraction experimentation to predict the change in performance when varying parameters. This proved to be of limited success as DELTAEC consistently predicted power

outputs vastly larger than what was observed. This can be seen in Figure 39 where experimental results are compared to DELTAEC theoretical power levels for the same set of parameters. The DELTAEC code for this plot can be seen in Appendix F. The sets of data were taken using the ND105-4 driver and the wedge placed in the ambient temperature duct. The temperature difference across the 5 cm, 100 cell/in² stack was approximately 400 °C. The power curve plots differ by a factor of thirty.

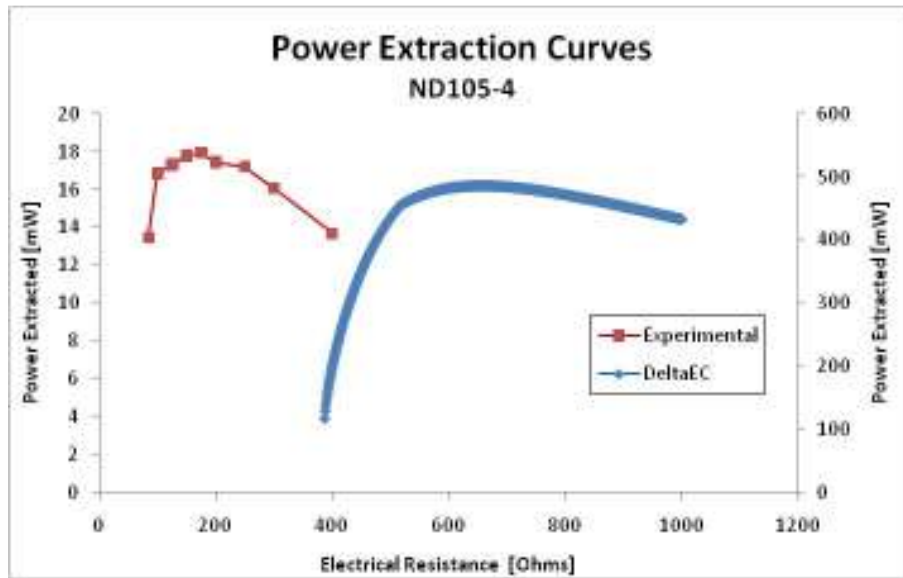


Figure 39: Experimental and DELTAEC power extraction curves. The DELTAEC data (•) corresponds to the right-side axis, and the experimental values (•) corresponds to the left axis. These sets of data both utilized the ND105-4 driver, the ambient temperature side duct wedge, the closer positioning of the ambient side heat exchanger. The experimental values of temperature for the hot and cool sides of the stack were input into the DELTAEC model. The temperature difference across the stack was approximately 400 °C.

CHAPTER 7 CONCLUSION

A small amount of electrical power was extracted from the half-engine design used in this proof-of-concept thesis project. This amount of power (between 18-24 mW) demonstrates that using air at atmospheric pressure can enable an inexpensive thermoacoustic engine, instead of the standard high-pressure noble gas (typically Helium), that are used as the thermodynamic working fluid. By analyzing the heat transfer through the thermoacoustic device, it was found that a second heat exchanger placed at the hot end of the Celcor stack, typical of most designs, was not required. The use of air at ambient pressure and only one heat exchanger will result in cheaper material costs and fewer geometric constraints. This conclusion could eventually push this technology closer to the production of commercially available, low-cost thermoacoustic cogenerator for use in biomass burning cook stoves.

With the completion of the testing on the half-engine design, the optimal parameters can be stated. These values were first investigated using the resonator in Helmholtz mode, and then further confirmed in power extraction mode. DELTAEC was used as much as possible to predict the trends in the performance of the resonator. These parameters aid the understanding of the physics behind the thermoacoustic engine and will be used to determine the design of future prototypes for this technology.

Between the three Celcor stack cell densities (400, 200, and 100 cell/in² corresponding to Lautrec numbers seen in Table 5), it was found that the 100 cell/in² Celcor ceramic stack was best for this design. Of the 10, 7.5, and 5 cm long stack lengths tested, the 5 cm length was found to be optimal. It was observed *via* pre-onset experimentation that mechanical resistance in the linear alternator played a very important role in the potential electrical power extraction from the resonator. The high levels of resistance in the Dayton DA115-8 drivers used initially dominated the energy loss in the resonator when being compared to the thermoviscous losses by nearly a factor of five. Because large amounts of mass had to be added to the loud speaker's cone to lower the frequency to an optimal value, it would make sense to use a moving magnet electro-acoustic transducer in the next prototype. Moving magnet transducers are also beneficial to the design because they also have relatively low mechanical losses. It was observed that volume exclusion in the ambient temperature side duct also played a very significant role in the performance of the resonator. The more volume excluded (wedge, plunger), the more power was extracted. All of these experimental observations will be utilized in future prototypes.

BIBLIOGRAPHY

¹T. R. Casten and P. F. Schewe, "Getting the Most from Energy", *Am. Sci.* **97**(1), 26-33 (Jan-Feb 2009).

²<http://www.freewatt.com/Technology/freewattpowergen.asp>.

³C. Lertsatitthanakorn, "Electrical performance analysis and economic evaluation of combined biomass cook stove thermoelectric (BITE) generator", *Bioresource Technology* **98**, 1670-1674 (2007).

⁴ <http://www.biolitestove.com/Biolite.html>

⁵A. C. Fernandez-Pello, *Proc. Combustion Inst.* **29**(1), 883-899 (2002).

⁶G. W. Swift, *Thermoacoustics: A Unifying Perspective for Some Engines and Refrigerators* (Acoustical Society of America, New York, 2002) ISBN 0-7354-0065-2.

⁷Shell Foundation "Building Spaces" program:
http://www.shellfoundation.org/pages/core_lines.php?p=corelines_content&page=breathing.

⁸Engineers in Technical and Humanitarian Opportunities of Service (ETHOS);
<http://improvedstoves.blogspot.com/2008/02/ethos-2008-conference.html>.

⁹Asian Regional Cook Stove Program (ARECOP); <http://www.arecop.org/>.

¹⁰"Smoke from Cooking Stoves Kills Poor People", *The Economist* (23 Sept 2010);
www.theeconomist.com/node/17093623?story_id=17093623.

¹¹K.R. Smith, S. Mehta and M. Maeusezahl-Feuz, "Indoor air pollution from household use of solid fuels" in *Comparative Quantification of Health Risks, Global and Regional Burden of Disease due to Selected Major Risk Factors*, Geneva, World Health Organization, Vol 2. pp. 1435-1493 (2004).

¹²B. A. Begum, *et al.*, "Indoor air pollution from particulate matter emissions in different households in rural areas of Bangladesh", *Building & Environment*, **44**(5), 898-903 (2009).

¹³P. Wilkinson, *et al.*, "Public Health Benefits of Strategies to Reduce Greenhouse-Gas Emission: Household Energy", *Lancet*, (25 Nov 2009); www.thelancet.com.

¹⁴WHO, "Fuel for Life: Household Energy and Health", Geneva, World Health Organization, 42 pp.

¹⁵The World Bank, *Meeting the Challenge for Rural Energy and Development*, VP for Finance and Private Sector Development, Industry & Energy Department, Washington, DC;
http://siteresources.worldbank.org/INTENERGY/Resources/Rural_Energy_Development_Paper_Improving_Energy_Supplies.pdf

¹⁶S. Szidat, "Sources of Asian Haze," *Science* **323**, 470-471 (23 Jan 2009);

- ¹⁷V. Ramanathan and G. Carmichael, "Global and regional climate changes due to black carbon", *Nature Geoscience* **1**, 221-227 (2008).
- ¹⁸E. Kintisch, "New Push Focuses on Quick Ways to Curb Global Warming", *Science*, **323**, 495-498 (23 Jan 2009).
- ¹⁹T. Friedman, *Hot, Flat, and Crowded* (Farrar, Straus and Giroux, 2008); ISBN 978-0-374-16685-4.
- ²⁰A. Jain, T. Rajeswara Rao, S. S. Sambhi and P. D. Grover, "Energy and chemicals from rice husks," *Biomass and Bioenergy* **7**(1-6), 285-289 (1995).
- ²¹A. T. Belonio, *The Rice Husk Gas Stove Handbook*, Appropriate Technology Center, Dept. Ag. Eng. and Enviro. Management, Central Philippine University, Iloilo City, Philippines (2005), 155 pages; http://stoves.bioenergylists.org/stovesdoc/Belonio/Belonio_gasifier.pdf.
- ²²N. MacCarty, D. Ogle, D. Still, T. Bond, C. Roden and B. Willson, *Laboratory Comparison of the Global-Warming Potential of Six Categories of Biomass Cooking Stoves*, Tech. Report, 26-pages, Aprovecho Research Center, Advanced Studies in Appropriate Technology, Creswell, OR (Sept. 2007).
- ²³ Roggema, "Philips Woodstove", *Appliance Magazine* (April 2007).
- ²⁴D. Mastbergen and B. Willson, "Generating light from stoves using a thermoelectric generator," Tech. Report, Engines and Energy Conversion Laboratory, Dept. Mechanical Engineering, University of Colorado (2007).
- ²⁵ C. Kittel, *Introduction to Solid State Physics*, 8th ed. (Wiley, 2004); ISBN 978-0471415268.
- ²⁶http://www.corning.com/environmentaltechnologies/products_services/ceramic_substrates.aspx.
- ²⁷A.B. Pippard, *The Physics of Vibration* (Cambridge Univ., 1989), Chpt. 11; ISBN 0 521 37200 3.
- ²⁸S. L. Garrett and R-L. Chen, "Build an 'Acoustic Laser'", *Echoes* **10**(3), 4-5 (2000).
- ²⁹S.L. Garrett, D.K. Perkins, A. Gopinath, "Thermoacoustic Refrigerator Heat Exchangers: Design, Analysis, and Fabrication", *Heat Transfer*, Proc. 10th Int. Heat Transfer Conf., Vol. IV, 375-380 (1994).
- ³⁰S.L. Garrett, "High Power Thermoacoustic Refrigerator", U.S. Pat. No. 5,647,216 (15 July 1997); South African Letters Pat. No.96/6512 (31 July 1996).
- ³¹G.W. Swift, *Thermoacoustics* (Acoustical Soc. Am., 2002), Sec. 7.2.1; ISBN 0 7354 0065 2.
- ³²Refractory firebrick, M^cMaster-Carr Part No. 9355K2, 200 Aurora Industrial Park, Aurora, OH 44202; www.mcmaster.com.
- ³³NiCr 80TM Alloy, Harrison Alloys, Inc., Harrison, NJ 07029.
- ³⁴Devcon Aluminum Liquid (F-2) epoxy #10710, ITW Devcon, 30 Endicott St., Danvers, MA 01923; www.devcon.com.

³⁵Vinyl caulk, McMaster-Carr Part No. 7649T12, 200 Aurora Industrial Park, Aurora, OH 44202; www.mcmaster.com.

³⁶R.S. Wakeland, "Heat Exchangers in Oscillating Flow, with Application to Thermoacoustic Devices that Have Neither Stack nor Regenerator", Thesis, Graduate Department in Acoustics, The Pennsylvania State University (2003).

³⁷*Parker O-Ring Handbook*, Pub. No. 5700, Parker Seal Group, O-Ring Division, 2360 Palumbo Drive, Lexington, KY 40512.

³⁸*Piezoresistive Pressure Transducer Instruction Manual*, Rep. IM8500 (Rev. B), Endevco, 30700 Rancho Viejo Rd., San Juan Capistrano, CA 92675-1748; www.endevco.com.

³⁹<http://www.parts-express.com>

⁴⁰Logan thermistor, Logan Enterprises, West Liberty, OH 43357, Part No. 4150-1/8-6-72-TH55033-RPS.

⁴¹T. J. Love, *Radiative Heat Transfer*, (C. E. Merrill, Ohio, 1968).

⁴²F. P. Incropera and D. P. DeWitt, *Fundamentals of Heat and Mass Transfer*, 3rd ed. (Wiley & Sons, 1990); ISBN 0-471-61246-4.

⁴³<http://www.corning.com/WorkArea/showcontent.aspx?id=6281>

⁴⁴<http://www.jxtianmei.com/esite/jxtianmei/default1.aspx?lan=en&catid=2&contentid=5>

⁴⁵S.L. Garrett, "Resource Letter: TA-1: Thermoacoustic Engines and Refrigerators", *Am. J. Phys.* **72**(1), 11-17 (2004).

APPENDIX A
Initial DELTAEC Model

```

1 C:\Users\Paul Montgomery\Documents\Penn State\Master's Thesis\DeltaEC Files\Dayt
2 This represents the first cut at half of a dual-differential standing wave
3 engine driving a conventional loudspeaker to generate electricity.
4 0 BEGIN Initial
5     9.8000E+04 a Mean P Pa
6 Gues     144.60 b Freq Hz
7 Gues     769.10 c TBeg K
8 Gues     3247.1 d |p| Pa
9     0.0000 e Ph(p) deg
0     0.0000 f |U| m^3/s
1     0.0000 g Ph(U) deg
2 Optional Parameters
3 air Gas type
4 1 SURFACE Hot End
5     3.0800E-03 a Area m^2
6     3247.1 A |p| Pa
7     0.0000 B Ph(p) deg
8     6.9697E-06 C |U| m^3/s
9     180.00 D Ph(U) deg
0     0.0000 E Htot W
1 ideal Solid type
2     -1.1316E-02 F Edot W
3 2 DUCT Hot Duct
4 Same 1a 3.0800E-03 a Area m^2
5     0.2600 b Perim m
6     9.2000E-02 c Length m
7     3209.5 A |p| Pa
8     1.9475E-02 B Ph(p) deg
9     6.1236E-03 C |U| m^3/s
0 Master-Slave Links
1     -90.563 D Ph(U) deg
2 Optional Parameters
3     0.0000 E Htot W
4 ideal Solid type
5     -9.9902E-02 F Edot W
6 3 HX Dummy Hot HX
7 Same 1a 3.0800E-03 a Area m^2
8 Same 4b 0.73933 b GasA/A
9     4.0000E-03 c Length m
0     1.0000E-03 d y0 m
1     30.000 e HeatIn W
2 Targ     800.00 f SolidT K
3 Master-Slave Links
4     769.10 G GasT K
5 ideal Solid type
6     800.00 H SolidT K
7 4 STRECT Celcor Stack (about 400 cells/in^2)
8 Same 1a 3.0800E-03 a Area m^2
9     0.73933 b GasA/A
0     9.5000E-02 c Length m
1     5.4600E-04 d aa m
2     8.9000E-05 e Lplate m
3 Same 4d 5.4600E-04 f bb m
4 Master-Slave Links
5 celcor Solid type
6     769.10 G TBeg K
7     316.93 H TEnd K
8 5 HX Ambient (boiling water cooled) HX
9 Same 1a 3.0800E-03 a Area m^2
0     0.8000 b GasA/A
1     1.0000E-02 c Length m
2     5.0000E-04 d y0 m
3 Gues     -31.244 e HeatIn W
4 Targ     310.00 f SolidT K
5 Master-Slave Links
6 copper Solid type
7     310.00 H SolidT K
    
```

5	6 RPW	Ambient HK gas stroke					
6		0.0000 a G or T			8.0828	A mm	
7		SC 2 * 5a / 5b / w / 1000 *					
8	7 DUCT	Zero Length Power Flow Monitor					
9		3.6600E-03 a Area m^2			2874.8	A p Pa	
10		0.3300 b Perim m			3.4121	B Ph(p) deg	
11		0.0000 c Length m			9.0472E-03	C U m^3/s	
12		Master-Slave Links			-78.83	D Ph(U) deg	
13		Optional Parameters			-1.2443	E Htot W	
14	ideal	Solid type			1.7552	F Edot W	
15	8 DUCT	Begin Ambient Duct					
16		Same 7a 3.6600E-03 a Area m^2			2862.0	A p Pa	
17		Same 7b 0.3300 b Perim m			3.3814	B Ph(p) deg	
18		5.0000E-03 c Length m			9.3950E-03	C U m^3/s	
19		5.0000E-04 d Srough			-78.127	D Ph(U) deg	
20		Master-Slave Links			-1.2443	E Htot W	
21		Optional Parameters			1.7526	F Edot W	
22	ideal	Solid type					
23	9 CONE	Wedge					
24		Same 8a 3.6600E-03 a AreaI m^2			2682.7	A p Pa	
25		Same 8b 0.3300 b PerimI m			3.0009	B Ph(p) deg	
26		3.3000E-02 c Length m			1.0726E-02	C U m^3/s	
27		9.7300E-04 d AreaF m^2			-80.125	D Ph(U) deg	
28		0.2939 e PerimF m			-1.2443	E Htot W	
29		5.0000E-04 f Srough			1.7220	F Edot W	
30		Master-Slave Links					
31		Optional Parameters					
32	ideal	Solid type					
33	10 DUCT	End of Ambient Duct					
34		Same 9d 9.7300E-04 a Area m^2			1791.1	A p Pa	
35		Same 9e 0.2939 b Perim m			0.66644	B Ph(p) deg	
36		7.6391E-02 c Length m			1.1855E-02	C U m^3/s	
37		5.0000E-04 d Srough			-80.938	D Ph(U) deg	
38		Master-Slave Links			-1.2443	E Htot W	
39		Optional Parameters			1.8475	F Edot W	
40	ideal	Solid type					
41	11 DUCT	Circular Duct					
42		3.4212E-03 a Area m^2	Mstr		1724.8	A p Pa	
43		0.20735 b Perim m	11a		0.36539	B Ph(p) deg	
44		1.9050E-02 c Length m			1.2587E-02	C U m^3/s	
45		5.0000E-04 d Srough			-81.462	D Ph(U) deg	
46		Master-Slave Links			-1.2443	E Htot W	
47		Optional Parameters			1.5432	F Edot W	
48	ideal	Solid type					
49	12 SPEAKER	Dayton DA115-8 4" Al Cone Woofer with Balsa weight					
50		5.3100E-03 a Area m^2			4.7860E-13	A p Pa	
51		6.4000 b R ohms			161.83	B Ph(p) deg	
52		7.0000E-04 c L H			1.2587E-02	C U m^3/s	
53		5.0000 d BLProd T-m			-81.475	D Ph(U) deg	
54		5.3000E-03 e M kg			4.4409E-16	E Htot W	
55		900.00 f K N/m			-1.8530E-15	F Edot W	
56		0.9500 g Rm N-s/m			1.2443	G WorkIn W	
57	Gues	0.1904 h I A			13.071	H Volts V	
58	Gues	98.525 i Ph(I) deg			0.1904	I Amps A	
59					0.53079	J Ph(2e) deg	
60					1724.8	K Pw Pa	
61	ideal	Solid type			-178.63	L Ph(Pw) deg	

```

2 13 RPN Impedance Magnitude and Stroke
3 0.0000 a G or T 5.2181 A mm
4 2.3704 B m/sec
5 1.7179E+05 C Pa-s/m^
6 4178.78639248 0.0243255592037 / 12C 12a / # w / 2000 *
7 14 RPN Electrical Impedance of alternator
8 (A) Imaginary Part
9 (B) Real Part
10 0.0000 a G or T 0.63598 A ohm
11 68.649 B ohm
12 12H 12I / 12J cos * 12H 12I / 12J sin *
13 15 RPN Target a resonance condition
14 TargSame 14A 0.63598 a G or T 0.63598 A ohm
15 12c w *
16 SOFTEND Open to air
17 Targ 0.0000 a Re(z) 4.7860E-13 A |p| Pa
18 Targ 0.0000 b Im(z) 161.83 B Ph(p) deg
19 Targ 0.0000 c Htot W 1.2587E-02 C |U| m^3/s
20 -81.475 D Ph(U) deg
21 4.4409E-16 E Htot W
22 -1.3530E-15 F Edot W
23 -2.3591E-16 G Re(z)
24 -4.6924E-16 H Im(z)
25 316.93 I T K
26 17 RPN ensure all ambient-duct dissipation goes to water jacket
27 0.0000 a G or T -2.9995 A watts
28 SE SF -

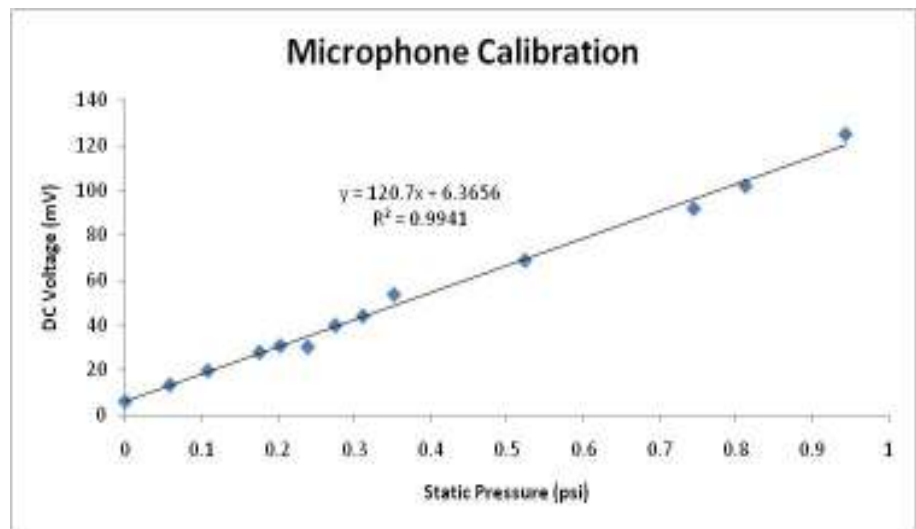
```

APPENDIX B

Piezo-resistive microphone calibration

The Endevco Model 8510B-2 (S/N: APJ50) piezoresistive differential pressure sensor is used as the resonator's internal microphone, located within one of the instrument doors on the side of the ambient temperature duct. The sensor's calibration was re-determined by attaching it to a water-filled U-tube and measuring the microphone's dc-output as a function of the level difference in the tube assuming water with a mass density of $\rho = 1.00 \text{ gm/cm}^3$ and a gravitational acceleration of $g = 9.806 \text{ m/sec}^2$.

Pressure psi	Mic Volt mV
0.944	125.0
0.813	102.0
0.745	92.0
0.524	69.0
0.352	53.8
0.312	44.3
0.275	40.1
0.239	30.6
0.203	31.1
0.176	28.2
0.108	20.0
0.059	13.7
0.000	6.4



This sensor was calibrated at Endevco on 12 June 1995 and had a sensitivity of 125.9 mV/psi.

APPENDIX C

Survey of commercially available 4" (nominal) drivers

Manufact.	Model	X_{max} (mm)	B/ (N/A)	Coil (mmφ)	Price (\$)	Comments	100 Hz V_{pk} (V/\$)	FOM Q_{ms} (V/\$)	R_m (Kg/sec)	m_o (gm)	f_o (Hz)	R_{dc} (Ω)	f_{max} (A _{pk})	I_{el} (W)	FOM (\$/W)	I_{diss} (W)	η_{el} (%)
Morel	EW428	4.5	6.1	54	148.20		17.2	0.12	2.36	6.16	62	6.3	1.37	5.90	25.11	1.44	80.4
Morel	CAW428	4.0	5.0	54			12.6	2.33	0.91	4.55	74	5.5	1.14	3.59		1.14	75.8
Morel	EM428				131.61												
Morel	MW113	3.0	4.0	54			7.5	3.13	0.80	5.54	72	6.2	0.61	1.15		0.75	60.3
Morel	MW114S	6.5	3.0	54			12.4	3.45	0.81	6.55	68	5.6	1.11	3.45		1.68	67.3
HIVI	B4N	3.2		25	17.20	Alcone											
Peerless	P830992	3.0	4.9	26	33.25		9.2	0.28	3.00	1.10	89	5.3	0.87	2.01	16.53	1.04	66.0
Peerless	P835023	3.1	5.0	26	38.22	Alcone	9.7	0.25	2.80	1.34	72	5.7	0.85	2.08	18.38	1.31	61.4
Peerless	830870	3.0	4.8	26	38.61	Polyprop.	9.0	0.23	3.19	0.90	73	5.2	0.87	1.97	19.62	0.85	69.9
Vifa	NE123W-04	3.0	4.4	32	62.82	Prelim.	8.3	0.13	6.70	0.38	65	3.3	1.26	2.61	24.11	0.36	87.8
Vifa	PL11WG09		4.9	25	32.50	4.5" o coil		2.20	1.20	5.90	69	5.6					
Tang Band	W4-1720	5.0	3.8	32	47.53		11.9	0.25	2.33	0.81	60	3.8	1.57	4.69	10.14	1.27	78.7
Tang Band	W4-1558SB	4.5	5.6	50	67.87		15.8	0.23	8.84	0.39	55	3.8	2.08	8.25	8.23	0.55	98.7
Dayton	DA115-3	2.5	5.7	25	14.56	Alcone	9.0	0.61	2.60	0.96	60	6.4	0.7	1.57	9.30	0.75	67.6
Dayton	ND105-4	4.0	3.9	25	12.00	Anodized Al	9.8	0.82	7.16	0.34	54	3.7	1.32	3.25	3.70	0.43	88.4
Dayton	ND105-8	4.0	4.9	25	24.85	Anodized Al	12.3	0.50	7.61	0.34	65	6.7	0.92	2.33	8.78	0.43	86.9
Parts Ex.	299-148	3.0		25	8.50	Polyprop.					105						

A comparison of various commercially-available 4" (nominal) loudspeakers that are evaluated as potential electrodynamic, moving-coil linear alternators for the thermoacoustic co-generator. Of critical importance is the rated peak displacement X_{max} and the product of magnetic flux density and coil length, $B\ell$, since those parameters determine the greatest possible output voltage $V_{pk} = 2\pi f B\ell X_{max}$. Also important is the speaker's mechanical dissipation that is characterized by Q_{ms} or the mechanical resistance R_m . By subtracting the mechanical power dissipated $I I_{diss} = \frac{1}{2} R_m v^2$, the maximum electro-acoustic conversion efficiency η_{el} could be calculated, if it was assumed that the load was matched to the voice coil's dc electrical resistance, R_{dc} .

APPENDIX D.1
Dayton DA115-8 manufacturer's specifications

DA 115-8

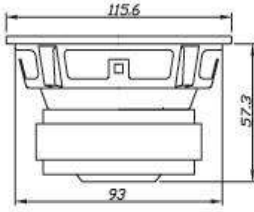
4" Aluminum Cone Woofer



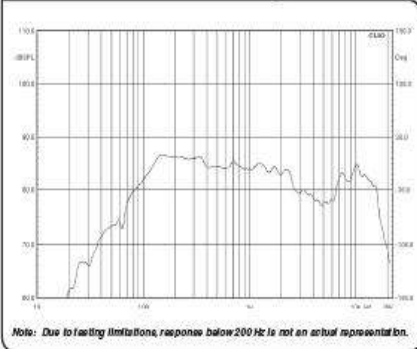


Features

- 4" one-piece aluminum cone
- Rubber surround
- Attractive steel frame
- High-damping composite dustcap
- Low distortion
- Extended frequency response

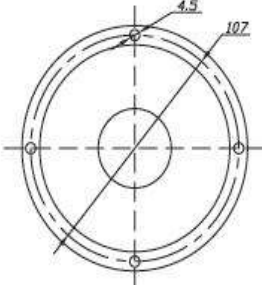


Frequency Response



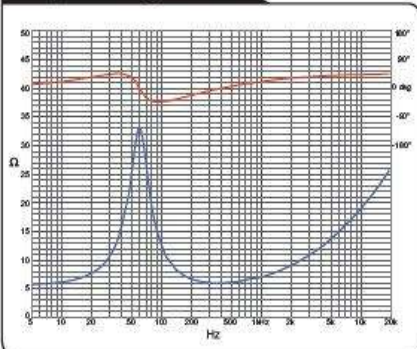
Note: Due to factory limitations, response below 200 Hz is not an actual representation.

Parameters	
Impedance (Ω)	8
Re (Ω)	6.4
Le (mH) @ 1 kHz	0.70
Fs (Hz)	60
Qms	2.6
Qes	0.49
Qts	0.41
Mms (g)	6.6
Cms (mm/N)	1.1
Sd (cm ²)	53.1
Vd (liters)	0.0133
BL (Tm)	5.7
VAS (liters)	4.4
XMAX (mm)	2.5
VC Diameter (mm)	51
SPL (dB @ 1W/1m)	84.9
RMS Power Handling (w)	20
Usable Frequency Range (Hz)	60 - 15,000



Note: All dimensions in mm.

Impedance/Phase



daytonaudio.com © Dayton Audio

APPENDIX D.2
Dayton ND105-4 manufacturer's specifications

ND105-4

ND105-4

4" Aluminum Cone Midbass Driver

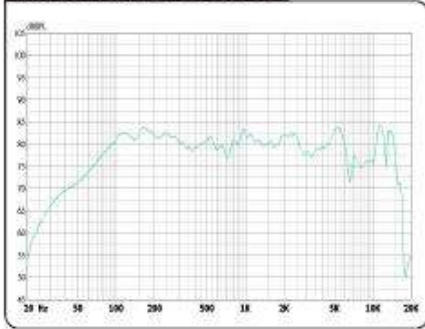


Features

- Low distortion Neo-Sym motor structure
- 4-Layer underhung voice coil
- Black anodized aluminum cone
- Low loss rubber surround
- X_{MAX} 4 mm / 20 mm peak
- Extended frequency range

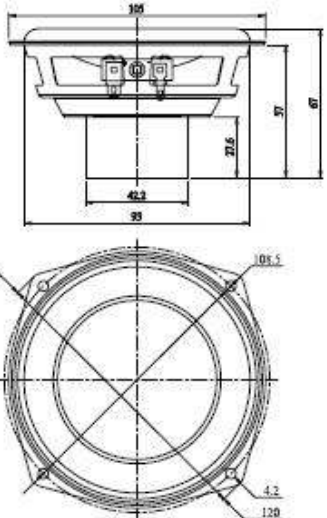


Frequency Response



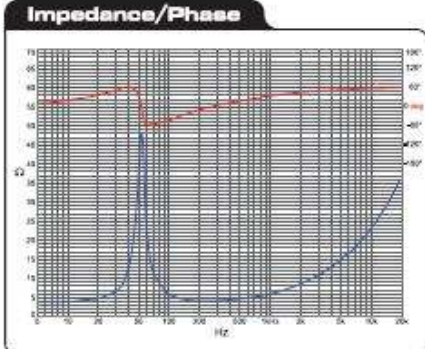
Parameters

Impedance (Ω)	4
Re (Ω)	3.7
Le (mH) @ 1 kHz	0.78
Fs (Hz)	53.8
Qms	7.16
Qes	0.59
Qts	0.55
Mms (g)	7.2
Cms (mm/N)	1.2
Sd (cm²)	51.5
Vd (cm³)	20.6
BL (Tm)	3.9
VAS (liters)	4.5
X _{MAX} (mm)	4
VC Diameter (mm)	25
SPL (dB@1W/1m)	82.6
RMS Power Handling (W)	30
Usable Frequency Range (Hz)	60 - 10,000



Note: All dimensions in mm.

Impedance/Phase



daytonaudio.com
© Dayton Audio Last Revised: 9/16/2010

APPENDIX E
 DELTAEC Model - Resonator in Helmholtz Model

```

1 C:\Users\Paul Montgomery\Documents\Penn State\Master's Thesis\DeltaEC Files\He
2 8/17/2010
3 0 BEGIN Initial
4 9.8000E+04 a Mean P Pa
5 Gues 149.44 b Freq Hz
6 Gues 578.21 c TBeg K
7 Gues 1.2771E+04 d |p| Pa
8 0.0000 e Ph(p) deg
9 0.0000 f |U| m^3/s
0 0.0000 g Ph(U) deg
1 Optional Parameters
2 air Gas type
3 1 SURFACE Hot End
4 3.0800E-03 a Area m^2 1.2771E+04 A |p| Pa
5 0.0000 B Ph(p) deg
6 2.1710E-05 C |U| m^3/s
7 180.00 D Ph(U) deg
8 0.0000 E Htot W
9 ideal Solid type -0.13863 F Edot W
0 2 RPN Length of Hot Duct
1 0.1920 a G or T 8.7000E-02 A m
2 4c 6c + 2a - -1 *
3 3 DUCT Hot Duct
4 Same 1a 3.0800E-03 a Area m^2 1.2583E+04 A |p| Pa
5 0.3200 b Perim m 2.3319E-02 B Ph(p) deg
6 Same 2A 8.7000E-02 c Length m 2.3502E-02 C |U| m^3/s
7 Master-Slave Links -90.521 D Ph(U) deg
8 Optional Parameters 0.0000 E Htot W
9 ideal Solid type -1.4048 F Edot W
0 4 HX Dummy Hot HX
1 Same 1a 3.0800E-03 a Area m^2 1.2550E+04 A |p| Pa
2 Same 6b 0.73933 b GasA/A 5.4769E-02 B Ph(p) deg
3 5.0000E-03 c Length m 2.4560E-02 C |U| m^3/s
4 1.0000E-03 d y0 m -90.683 D Ph(U) deg
5 Gues 210.71 e HeatIn W 210.71 E Htot W
6 Master-Slave Links -1.9843 F Edot W
7 Possible targets 578.21 G GasT K
8 ideal Solid type 743.00 H SolidT K
9 5 RPN ChangeMe
0 Targ 743.00 a G or T 743.00 A ChngMe
1 4H
2 6 STKRECT Celcor Stack (about 400 cells/in^2) less Dummy HX length
3 Same 1a 3.0800E-03 a Area m^2 1.1005E+04 A |p| Pa
4 0.73933 b GasA/A 6def 3.9004 B Ph(p) deg
5 0.1000 c Length m 3.9607E-02 C |U| m^3/s
6 5.4600E-04 d aa m Mstr -82.781 D Ph(U) deg
7 8.9000E-05 e Lplate m Mstr 210.71 E Htot W
8 Same 6d 5.4600E-04 f bb m Mstr 12.615 F Edot W
9 Master-Slave Links 578.21 G TBeg K
0 celcor Solid type 311.73 H TEnd K
1 7 HX Ambient (Intel Fin) HX
2 3.6300E-03 a Area m^2 1.0836E+04 A |p| Pa
3 0.8100 b GasA/A 4.0627 B Ph(p) deg
4 1.0000E-02 c Length m 4.1989E-02 C |U| m^3/s
5 5.0000E-04 d y0 m -83.249 D Ph(U) deg
6 Gues -200.04 e HeatIn W 10.669 E Htot W
7 Targ 283.00 f SolidT K 10.669 F Edot W
8 Master-Slave Links 311.73 G GasT K
9 copper Solid type 283.00 H SolidT K
0 8 RPN Ambient HX gas stroke
1 0.0000 a G or T 30.417 A mm
2 7C 2 * 7a / 7b / w / 1000 *
    
```

3	9 ANCHOR	subsequent duct is ambient temperature									
4	10 DUCT	Begin Ambient Duct									
5		3.6600E-03	a	Area	m ²	1.0776E+04	A p	Pa			
6		0.3300	b	Perim	m	4.0507	B Ph(p)	deg			
7		5.0000E-03	c	Length	m	4.3346E-02	C U	m ³ /s			
8		5.0000E-04	d	Srough		-83.341	D Ph(U)	deg			
9	Master-Slave Links										
10	Optional Parameters										
11	ideal	Solid type							10.627	F Edot	W
2	11 CONE	Wedge									
3	Same 10a	3.6600E-03	a	AreaI	m ²	9916.7	A p	Pa			
4	Same 10b	0.3300	b	PerimI	m	3.9434	B Ph(p)	deg			
5		3.3000E-02	c	Length	m	4.8543E-02	C U	m ³ /s			
6		9.7300E-04	d	AreaF	m ²	-83.666	D Ph(U)	deg			
7		0.2939	e	PerimF	m	10.041	E Htot	W			
8		5.0000E-04	f	Srough		10.041	F Edot	W			
9	Master-Slave Links										
10	Optional Parameters										
11	ideal	Solid type							10.627	F Edot	W
2	12 DUCT	End of Ambient Duct									
3	Same 11d	9.7300E-04	a	Area	m ²	5765.9	A p	Pa			
4	Same 11e	0.2939	b	Perim	m	4.0720	B Ph(p)	deg			
5		7.6391E-02	c	Length	m	5.2617E-02	C U	m ³ /s			
6		5.0000E-04	d	Srough		-83.93	D Ph(U)	deg			
7	Master-Slave Links										
8	Optional Parameters										
9	ideal	Solid type							5.2877	F Edot	W
0	13 DUCT	Circular Duct									
1		3.4212E-03	a	Area	m ²	5455.7	A p	Pa			
2		0.20735	b	Perim	m	3.9804	B Ph(p)	deg			
3		1.9050E-02	c	Length	m	5.5125E-02	C U	m ³ /s			
4		5.0000E-04	d	Srough		-84.031	D Ph(U)	deg			
5	Master-Slave Links										
6	Optional Parameters										
7	ideal	Solid type							5.2192	F Edot	W
8	14 DUCT	Helmholtz Resonator Pipe									
9		5.4300E-04	a	Area	m ²	8.7278E-11	A p	Pa			
0		8.2605E-02	b	Perim	m	-168.39	B Ph(p)	deg			
1		5.2000E-02	c	Length	m	5.5661E-02	C U	m ³ /s			
2		5.0000E-04	d	Srough		-84.058	D Ph(U)	deg			
3	Master-Slave Links										
4	Optional Parameters										
5	ideal	Solid type							2.3991E-13	F Edot	W
6	15 SOFTEND	Open to air									
7	Targ	0.0000	a	Re(z)		8.7278E-11	A p	Pa			
8	Targ	0.0000	b	Im(z)		-168.39	B Ph(p)	deg			
9						5.5661E-02	C U	m ³ /s			
0						-84.058	D Ph(U)	deg			
1						2.3991E-13	E Htot	W			
2						2.3991E-13	F Edot	W			
3						2.1695E-16	G Re(z)				
4						-2.1858E-15	H Im(z)				
5						311.73	I T	K			
6	16 RPN	ensure all ambient-duct dissipation goes to water jacket									
7	Targ	0.0000	a	G or T		1.4211E-13	A watts				
8	7E 7F -										

APPENDIX F
 DELTAEC code for Resonator in Power Extraction mode

```

1 C:\Users\Paul Montgomery\Documents\Penn State\Master's Thesis\DeltaEC Files\njnj Stove 1
2 Represents the final design as of 1 October 2010.
3 0 BEGIN Initial
4 9.8000E+04 a Mean P Pa
5 Gues 50.907 b Freq Hz
6 Gues 616.71 c TBeg K
7 Gues 2151.1 d |p| Pa
8 0.0000 e Ph(p) deg
9 0.0000 f |U| m^3/s
10 0.0000 g Ph(U) deg
11 Optional Parameters
12 air Gas type
13 1 SURFACE Hot End
14 3.0800E-03 a Area m^2 2151.1 A |p| Pa
15 0.0000 B Ph(p) deg
16 2.2595E-06 C |U| m^3/s
17 180.00 D Ph(U) deg
18 0.0000 E Htot W
19 ideal Solid type -2.4303E-03 F Edot W
20 2 RPN Hot Duct Length Calc
21 0.1620 a G or T 0.1120 A m
22 2a 7c -
23 3 DUCT Hot Duct
24 Same 1a 3.0800E-03 a Area m^2 2145.5 A |p| Pa
25 0.3200 b Perim m 7.6020E-03 B Ph(p) deg
26 Same 2A 0.1120 c Length m 1.7549E-03 C |U| m^3/s
27 Master-Slave Links -90.917 D Ph(U) deg
28 Optional Parameters 0.0000 E Htot W
29 ideal Solid type -3.0370E-02 F Edot W
30 4 RPN Half-stroke of gas within hot HK
31 0.0000 a G or T 2.4545E-03 A m
32 3C 5a / w / 5b /
33 5 HK Dummy Hot HK
34 Same 1a 3.0800E-03 a Area m^2 2144.5 A |p| Pa
35 Same 7b 0.72576 b GasA/A 1.8438E-02 B Ph(p) deg
36 5.0000E-03 c Length m 1.8206E-03 C |U| m^3/s
37 1.0000E-03 d y0 m -91.158 D Ph(U) deg
38 Gues 27.833 e HeatIn W 27.833 E Htot W
39 Master-Slave Links -4.0075E-02 F Edot W
40 Possible targets 616.71 G GasT K
41 ideal Solid type 654.99 H SolidT K
42 6 RPN Target Hot-Side Temperature
43 Targ 738.00 a G or T 654.99 A K
44 5H
45 7 STRRECT Calcscr Stack 200 cpsi
46 Same 1a 3.0800E-03 a Area m^2 2127.9 A |p| Pa
47 0.72576 b GasA/A 7def 0.28263 B Ph(p) deg
48 5.0000E-02 c Length m 1.5975E-03 C |U| m^3/s
49 7.6800E-04 d aa m Mstr -71.252 D Ph(U) deg
50 1.3250E-04 e Lplate m Mstr 27.833 E Htot W
51 Same 7d 7.6800E-04 f bb m Mstr 0.53972 F Edot W
52 Master-Slave Links 616.71 G TBeg K
53 celcor Solid type 170.44 H TEnd K
54 8 HK Ambient (Inbel Fin) HK
55 3.6300E-03 a Area m^2 2125.5 A |p| Pa
56 0.8100 b GasA/A 0.22392 B Ph(p) deg
57 1.0000E-02 c Length m 1.7445E-03 C |U| m^3/s
58 5.0000E-04 d y0 m -73.512 D Ph(U) deg
59 Gues -27.308 e HeatIn W 0.52496 E Htot W
60 Targ 340.00 f SolidT K 0.52496 F Edot W
61 Master-Slave Links 170.44 G GasT K
62 copper Solid type 151.95 H SolidT K
  
```

93	9 RPN	Ambient HK gas stroke				
94		0.0000 a G or T		3.7098	A mm	
95		BC 2 + 8a / 8b / w / 1000 +				
96	10 ANCHOR	subsequent duct is ambient temperature				
97	11 DUCT	Ambient Duct				
98		3.6600E-03 a Area m^2		2037.4	A p Pa	
99		0.3300 b Perim m		-0.13539	B Ph(p) deg	
100		0.1576 c Length m		4.5156E-03	C U m^3/s	
101		5.0000E-04 d Strough		-83.744	D Ph(U) deg	
102		Master-Slave Links		0.5121	E Htot W	
103		Optional Parameters		0.5121	F Edot W	
104		ideal Solid type				
105	12 RPN	Electrical Load Re to Mechanical Resistance Rm				
106		OP1t 100.00 a G or T		1.4498	A Kg/sec	
107		15d 15d + 12a / 0.499 +				
108	13 RPN	Added Mass to Driver				
109		45.000 a G or T		5.1850E-02	A kg	
110		13a 1000 / 0.00685 +				
111	14 VOLUME	Volume of ambient-side duct with wedge.				
112		3 b BegSeg		1.1275E-03	A TotVol m^3	
113		11 c EndSeg				
114		Possible targets				
115	15 IESPEAKER	Dayton ND105-4 #3				
116		5.3100E-03 a Area m^2		5.8567	A p Pa	
117		4.0920 b R ohms		96.243	B Ph(p) deg	
118		7.0000E-04 c L H		4.5154E-03	C U m^3/s	
119		9.7510 d BLProd T-m		-83.758	D Ph(U) deg	
120		Same 13a 5.1850E-02 e M kg		-1.3223E-02	E Htot W	
121		1260.5 f K N/m		-1.3223E-02	F Edot W	
122		Same 12a 1.4498 g Rm N-s/m		0.0000	G WorkIn W	
123		0.0000 h I A		8.2919	H Volts V	
124		0.0000 i Ph(I) deg		0.0000	I Amps A	
125				96.243	J Ph(Ze) deg	
126				2038.1	K Pw Pa	
127		ideal Solid type		179.70	L Ph(Pw) deg	
128	16 RPN	Impedance Magnitude and Stroke				
129		(A) Speaker stroke				
130		(B) Speaker velocity				
131		(C) Magnitude of speak acoustic impedance				
132		0.0000 a G or T		5.3171	A mm	
133				0.85036	B m/sec	
134				4.5120E+05	C Pa-s/m3	
135		11A 11C / 15C 15a / # w / 2000 +				
136	17 RPN	Power delivered to external load resistor				
137		0.0000 a G or T		100.00	A ohms	
138				0.31728	B watts	
139		15H 15b 12a + / # + 12a + 2 / 12a				
140	18 SOFTEND	Open to air				
141	Targ	0.0000 a Re(s)		5.8567	A p Pa	
142	Targ	0.0000 b Im(s)		96.243	B Ph(p) deg	
143				4.5154E-03	C U m^3/s	
144				-83.758	D Ph(U) deg	
145				-1.3223E-02	E Htot W	
146				-1.3223E-02	F Edot W	
147				-1.3138E-02	G Re(s)	
148				-7.0723E-08	H Im(s)	
149				170.44	I T K	
150	19 RPN	ensure all ambient-duct dissipation goes to water jacket				
151	Targ	0.0000 a G or T		-1.0054E-07	A watts	
152		EE 8F -				